Successful Common Envelope Ejection and Binary Neutron Star Formation in 3D Hydrodynamics

Jamie A. P. Law-Smith [ID],[1,2] Rosa Wallace Everson [ID],[1,2,*] Enrico Ramirez-Ruiz [ID],[1,2] Selma E. de Mink [ID],[3,4,5]
Lieke A. C. van Son [ID],[3,5] Ylva Götberg [ID],[6,7] Stefan Zellmann [ID],[8] Alejandro Vigna-Gómez [ID],[2]
Mathieu Renzo [ID],[9,10] Samantha Wu [ID],[11] Sophie L. Schrøder [ID],[2] Ryan J. Foley [ID],[1] and
Tenley Hutchinson-Smith [ID][1,2]

[1]Department of Astronomy and Astrophysics, University of California, Santa Cruz, CA 95064, USA
[2]Niels Bohr Institute, University of Copenhagen, Blegdamsvej 17, 2100 Copenhagen, Denmark
[3]Harvard-Smithsonian Center for Astrophysics, Harvard University, 60 Garden St, Cambridge, MA 02138, USA
[4]Max-Planck-Institut für Astrophysik, Karl-Schwarzschild-Straße 1, 85740 Garching bei München, Germany
[5]Anton Pannekoek Institute for Astronomy, University of Amsterdam, Science Park 904, 1098XH Amsterdam, The Netherlands
[6]The observatories of the Carnegie institution for science, 813 Santa Barbara Street, Pasadena, CA 91101, USA
[7]Kavli Institute for Theoretical Physics, University of California, Santa Barbara, CA 93106, USA
[8]Institute of Computer Science, University of Cologne, Weyertal 121, 50931 Cologne, Germany
[9]Center for Computational Astrophysics, Flatiron Institute, New York, NY 10010, USA
[10]Department of Physics, Columbia University, New York, NY 10027, USA
[11]California Institute of Technology, 1200 East California Boulevard, MC 249-17, Pasadena, CA 91125, USA

ABSTRACT

The coalescence of two neutron stars was recently observed in a multi-messenger detection of gravitational wave (GW) and electromagnetic (EM) radiation. Binary neutron stars that merge within a Hubble time, as well as many other compact binaries, are expected to form via common envelope evolution. Yet five decades of research on common envelope evolution have not yet resulted in a satisfactory understanding of the multi-spatial multi-timescale evolution for the systems that lead to compact binaries. In this paper, we report on the first successful simulations of common envelope ejection leading to binary neutron star formation in 3D hydrodynamics. We simulate the dynamical inspiral phase of the interaction between a $12M_\odot$ red supergiant and a $1.4M_\odot$ neutron star for different initial separations and initial conditions. For all of our simulations, we find complete envelope ejection and a final orbital separation of ≈ 1.1–$2.8R_\odot$, leading to a binary neutron star that will merge within 0.01–1 Gyr. We find an $\alpha_{\rm CE}$-equivalent efficiency of ≈ 0.1–0.4 for the models we study, but this may be specific for these extended progenitors. We fully resolve the core of the star to $\lesssim 0.005R_\odot$ and our 3D hydrodynamics simulations are informed by an adjusted 1D analytic energy formalism and a 2D kinematics study in order to overcome the prohibitive computational cost of simulating these systems. The framework we develop in this paper can be used to simulate a wide variety of interactions between stars, from stellar mergers to common envelope episodes leading to GW sources.

Keywords: neutron stars—gravitational waves—common envelope—stellar evolution—hydrodynamics

1. INTRODUCTION

Until now, the majority of astrophysical sources detected by the advanced Laser Interferometer Gravitational-Wave Observatory (LIGO) and Virgo

Corresponding author: Jamie A. P. Law-Smith
lawsmith@ucsc.edu

* NSF Graduate Research Fellow

observatory have involved stellar mass binary black hole (BBH) mergers, with the two most notable exceptions being the (likely) binary neutron star (BNS) mergers GW170817 and GW190425 (Abbott et al. 2017a, 2020). While dynamical encounters may play a role in the origin of BBHs, they are not an effective pathway for the assembly of binary neutron star mergers (e.g., Ye et al. 2020), which are thought to form almost exclusively in interacting binaries (Tutukov & Yungelson 1973, 1993; Belczynski et al. 2016).

Massive stars are the progenitors of neutron stars and black holes, and the majority of massive (i.e., type B and O) stars are in interacting binaries (Sana et al. 2012; Moe & Di Stefano 2017). A BNS is expected to form from the cores of well-evolved stars, and thus have much lower orbital energy and angular momentum than the original binary progenitor. For BNSs that merge in a Hubble time, after one of the progenitor stars evolves through the red giant phase and overflows its Roche lobe, the original binary is believed to significantly shrink during a phase of unstable mass transfer, which leads to a spiral-in of the binary and ejection of the envelope—this is collectively commonly referred to as common envelope (CE) evolution (e.g., Ritter 1975; Paczynski 1976; Iben & Livio 1993; Ivanova et al. 2013b). If this process leads to a deposition of orbital energy that is sufficient to eject the envelope of the giant, the predicted properties of the resulting compact binary could match the observed properties of the BNS population. Past attempts to model this process have failed because they cannot reproduce these observed properties. A more complete (and in particular, multidimensional) theoretical description is required in order to provide an accurate description of the evolution of a NS embedded in a common envelope. This work focuses on the decades-long pursuit of this elusive phenomenon.

A critical juncture in the life of a binary occurs just after mass transfer commences in the system. The system either coalesces or may survive to become an interacting binary. This is the case of the recently discovered M Supergiant High Mass X-Ray Binary (HMXB) 4U 1954+31 (Hinkle et al. 2020), which contains a late-type supergiant of mass $9^{+6}_{-2}M_\odot$; it is the only known binary system of its type. It is difficult and rare to observe a system in this state, as the system evolves rapidly, yet this discovery may be the first observation of a system similar to the progenitor studied in this work. If mass transfer becomes unstable in this system it could lead to a CE episode. Two outcomes are then possible: (1) one star has a clear core/envelope separation and the other star is engulfed into its envelope, or (2) both stars have a core/envelope separation and the envelopes of the two stars overfill their Roche lobes. Usually, the term CE is used to describe a situation in which the envelope is not co-rotating with the binary and is not necessarily in hydrostatic equilibrium. The state of the primary at onset of CE evolution is determined by the initial separation and the orbital evolution of the binary—generally, it will begin when the radius of the primary overflows its Roche lobe. The outcome of the CE phase can be either a stellar merger or the formation of close binary. If the latter,

this tightened binary has an associated merger timescale from gravitational-wave (GW) dissipation that depends on the final orbital separation and energy of the binary. If these are small enough such that the binary merges within a Hubble time, the stellar remnants—either black holes, neutron stars, or white dwarfs—will merge and produce GW and possibly electromagnetic (EM) radiation.

In particular, BNS mergers expel metallic, radioactive debris (the light from which is referred to as a kilonova) that can be seen by telescopes (e.g., Kasen et al. 2017). In August 2017, for the first time, we detected both GWs and EM radiation (Coulter et al. 2017; Abbott et al. 2017b; Goldstein et al. 2017) coming from the same astrophysical event. This landmark discovery, which has opened up new lines of research into several areas in astrophysics and physics, makes the study of interacting binaries and common envelope in particular, even more essential in our attempts to discern the assembly history of these probes of extreme physics. Yet, their formation process remains an open question.

In this work we present the first 3D hydrodynamics simulations of successful CE ejection leading to a BNS system. Simulations of this kind have not been performed so far due to the prohibitive computational cost—the relevant dynamic ranges of density and physical distance are $\gtrsim 10^6$ (e.g., the global problem must resolve a $R \approx 10^6$ cm neutron star within the envelope of a $R \approx 10^{13}$ cm giant star, whose density varies from $\rho \approx 10^6$ g/cm^3 to $\rho \approx 10^{-9}$ g/cm^3 within the relevant regions). Most 3D hydrodynamics simulations of CE evolution have been at relatively equal mass ratios and for relatively low stellar masses ($M_\star \lesssim 3M_\odot$) (e.g., Zhang & Fryer 2001; Ricker & Taam 2008, 2012; Nandez & Ivanova 2016; Ohlmann et al. 2016; Prust & Chang 2019; Kramer et al. 2020; Sand et al. 2020; Chamandy et al. 2020), and there has been an early attempt and characterization of the difficulties faced by simulating a massive star binary by Ricker et al. (2019). Higher mass ratios involving NSs have been studied in 1D (e.g., MacLeod & Ramirez-Ruiz 2015; Fragos et al. 2019).

In contrast to other contemporary studies, the initial conditions of our 3D hydrodynamics simulations are informed by an adjusted 1D analytic energy formalism and a 2D kinematics study. We start the 3D hydrodynamics simulation once the secondary has reached a relatively small radius (after ejecting $< 0.1\%$ of the star's binding energy, at $r \approx 10R_\odot$) compared to the full radius of the star. In contrast to other contemporary work in which the core is often replaced with a point mass, we fully resolve the core to $\lesssim 0.005R_\odot$.

This paper is organized as follows. §2 describes our methods, including the 1D analysis, 2D kinematics, and 3D hydrodynamics, §3 describes our results, §4 compares to other work and discusses caveats and future work, and §5 concludes.

2. METHODS

We simulate the CE evolution of an initially $12M_\odot$ red supergiant primary (donor) and a $1.4M_\odot$ point mass secondary (NS) in 3D hydrodynamics, for different initial separations and initial conditions. We build the primary with a 1D stellar evolution code (MESA). We use an adjusted 1D energy formalism to predict the likely CE ejection regime, and we use a 2D kinematics study to inform the initial conditions of the 3D hydrodynamics simulations. We import the stellar model to the 3D hydrodynamics simulation (FLASH), in which we excise the outermost layers of the star with negligible binding energy and start the secondary relatively close to the core of the primary where the CE ejection is predicted to take place.

2.1. MESA model

We use the 1D stellar evolution code MESA v8118 (Paxton et al. 2011, 2013, 2015) to construct the primary. We use an inlist from Götberg et al. (2018), which is publicly available on Zenodo.[1] We construct a $12M_\odot$ solar-metallicity (X=0.7154, Y=0.270, Z=0.0142; Asplund et al. 2009) primary as this is a typical mass to form a NS (Heger et al. 2003). In §3 we show the evolutionary history of this model and in §C and §D we show mass, density, composition, and binding energy profiles for the models we simulate in 3D hydrodynamics.

See Section 2.1 of Götberg et al. (2018) for details on the MESA setup. Additional uncertainties in the MESA modeling are discussed in Section 4. In brief, our setup is to use the `mesa_49.net` nuclear network of 49 isotopes, account for overshooting following Brott et al. (2011), and account for mass loss using the wind schemes of de Jager et al. (1988) and Vink et al. (2001).

2.2. Energy formalism

We perform CE energy formalism (α formalism; Livio & Soker 1988; van den Heuvel 1976; Webbink 1984; de Kool 1990; Iben & Livio 1993) calculations on the profiles to predict the radius ranges in which CE ejection is possible and to inform the initial conditions of the 3D hydrodynamics simulations. As in Wu et al. (2020), we calculate the gravitational binding energy and orbital

---

energy loss profiles (see §D) for the MESA model at all ages throughout its giant branch evolution. These profiles help determine the predicted ejection ranges (see §3). See Wu et al. (2020) and Everson et al. (2020) for further details of these calculations.

Local 3D hydrodynamical simulations of CE have shown that during dynamical inspiral, the energy deposition from the secondary's plunge extends inward from the secondary's location, heating and unbinding deeper envelope material (see, e.g., MacLeod et al. 2017a; De et al. 2020). To incorporate the effects of this energy deposition on the ejection radius range, we also apply an adjusted α formalism (Everson 2020) that requires the orbital energy loss to overcome the binding energy at radii deeper than that given by the orbital separation, corresponding to $r - R_a$ (where R_a is the Bondi accretion radius) or $r - R_{\rm Roche}$ (where $R_{\rm Roche}$ is the Roche radius); see below. The ejection ranges shown in Figure 1 were calculated using this adjusted α formalism as well as using work from Everson et al. (2020).

All α formalism calculations in, e.g., Figure 10, are based on, e.g., Ivanova et al. (2013b) and Kruckow et al. (2016). The change in orbital energy is defined as in Eqn. 2 of Kruckow et al. (2016):

$$\Delta E_{\rm orb} = -\frac{GM_{\rm core}M_{\rm secondary}}{2a_{\rm f}} + \frac{GM_{\rm donor}M_{\rm secondary}}{2a_{\rm i}},$$
(1)

where $a_{\rm i}$ is the initial orbital separation and $a_{\rm f}$ is the final orbital separation, and the gravitational binding energy is defined as

$$E_{\rm bind} = -\int \frac{Gm}{r}dm.$$
(2)

For the $r - R_a$ adjusted formalism we use the accretion radius as defined in, e.g., Bondi & Hoyle (1944) and Hoyle & Lyttleton (1939):

$$R_a = \frac{2GM_{\rm secondary}}{v_\infty^2}$$
(3)

and for the $r - R_{\rm Roche}$ adjusted formalism we use the Roche radius (the radius equivalent to the volume of the Roche lobe) as in the approximation of Eggleton (1983).

We adapted a 2D integrator used to study the kinematics of CE inspiral with drag (MacLeod et al. 2017a) with the results from a 3D study of drag coefficients in CE evolution with density gradients (De et al. 2020) to determine an initial velocity vector for the radius at which we begin our 3D hydrodynamics simulations. We also compare to results a circular initial velocity vector.

2.3. FLASH setup

The outline of our 3D hydrodynamics setup is the following: (1) excise the tenuous outer layers of the primary (donor) star, (2) initialize the primary on the grid, (3) relax the point particle secondary (neutron star) onto the grid, (4) initialize the point particle's velocity vector based on the 2D kinematics results, and (5) simulate the system in 3D hydrodynamics until the orbital separation stalls and "parks".

In this paper, we focus on evolutionary stages which we expect that will lead to a CE ejection *a priori* and then use 3D hydrodynamics to simulate the crucial dynamical inspiral phase of the CE evolution.

Numerical diffusion prohibits us from evolving the system for $\gtrsim 30$ orbits, since for many orbits, numerically-driven drag results in the companion inspiraling toward the core of the donor. See §4 for a detailed discussion of this. Thus, we consider only evolution in the 3D hydrodynamics on a timescale much shorter than the thermal timescale, to prevent including artificially merging or ejected cases.

We use a custom setup of the 3D adaptive-mesh refinement (AMR) hydrodynamics code FLASH (Fryxell et al. 2000), version 4.3[2]. Our FLASH setup is based on that of Wu et al. (2020), which was based on that of Law-Smith et al. (2019) and Law-Smith et al. (2020), which was in turn based on that of Guillochon et al. (2009) and Guillochon & Ramirez-Ruiz (2013). See these references for more details on the numerics. A brief summary including salient features and changes to the setup is below.

We use an Helmholtz equation of state with an extended Helmholtz table[3] spanning $10^{-12} \leq \rho \,[\mathrm{g\ cm^{-3}}] \leq 10^{15}$ and $10^3 \leq T \,[\mathrm{K}] \leq 10^{13}$. The Helmholtz equation of state assumes full ionization (Timmes & Swesty 2000) and thus does not include recombination energy in the internal energy. We track the same chemical abundances in the 3D hydrodynamics as in the MESA nuclear network for the star, for all elements above a mass fraction of 10^{-5} (this value is somewhat arbitrary but does not affect the results); this is 22 elements ranging from hydrogen (^{1}H) to iron (^{56}Fe). While including an arbitrary number of the elements tracked in MESA is possible, including all of the elements would unnecessarily increase the memory load of the 3D hydrodynamics.

We excise the outer envelope of the primary donor star, which constitutes $< 0.1\%$ of the total binding energy (see §2.2, §3, and §C for further discussion) and is easily ejected, trimming the star to $R = 10R_\odot$. Our

box size is $\Delta X_{\max} = 40R_\odot$ on a side. This technique was also employed in Wu et al. (2020). We refine such that $\Delta X_{\min} \lesssim 0.005R_\odot$ within a factor of 100 of the maximum density, then derefine in the AMR with decreasing density, for $N \approx 272$ cells across the diameter of the star for the nominal simulations presented in this paper. We verified the hydrostatic equilibrium of our initial conditions for several dynamical timescales of the star (and 100s of dynamical timescales of the core). Hydrostatic equilibrium following the relaxation scheme in our setup has also been tested in e.g., Law-Smith et al. (2020). We initialize the secondary point mass (NS) at $r = 8R_\odot$, well within the envelope of the $10R_\odot$ trimmed star. After initializing the star on the grid, we gradually introduce the point mass secondary inside the envelope of the primary by gradually increasing its velocity to its initial velocity vector (see also §2.2). This technique is also used in MacLeod et al. (2017a) and Wu et al. (2020).

More realistic initial conditions would start at the point of Roche lobe overflow to take into account the transfer of energy and angular momentum from the orbit to the envelope, but this is computationally prohibitive for a $R_\star \approx 1000R_\odot$ primary with a density range over 15 orders of magnitude (from $\rho \approx 10^6$ to $\rho \approx 10^{-9}$ g/cm^3). However, we argue that the initial conditions used in this work are similar to the configuration if we had begun the simulation at this earlier stage and evolved it to the time we start our simulation. This is justified in §C and using the methods of §2.2.

We use two initial velocity vectors: (1) circular and (2) informed by a 2D kinematics study using the stellar density profile. The 2D kinematics velocity vectors are derived from orbits that are more eccentric than a circular orbit. However, we find that the initial velocity vector does not have a significant effect on the final outcome of the simulation, with both velocity vectors leading to qualitatively similar results. This weak dependence on the initial velocity vector is due to the fact that the point mass relatively quickly encounters drag and spirals inward dynamically, as was also found in Wu et al. (2020).

We also perform a numerical convergence study (see §G for details). For this, we run two simulations with the same initial conditions but one with 2.5 times higher linear resolution than the other, and find very similar results in the orbital evolution and energy of the envelope, verifying that our nominal resolution of $\Delta X_{\min} \lesssim 0.005R_\odot$ is converged.

---

[2] The updates in later versions do not affect our setup.

[3] As of time of writing available at http://cococubed.asu.edu/code_pages/eos.shtml.
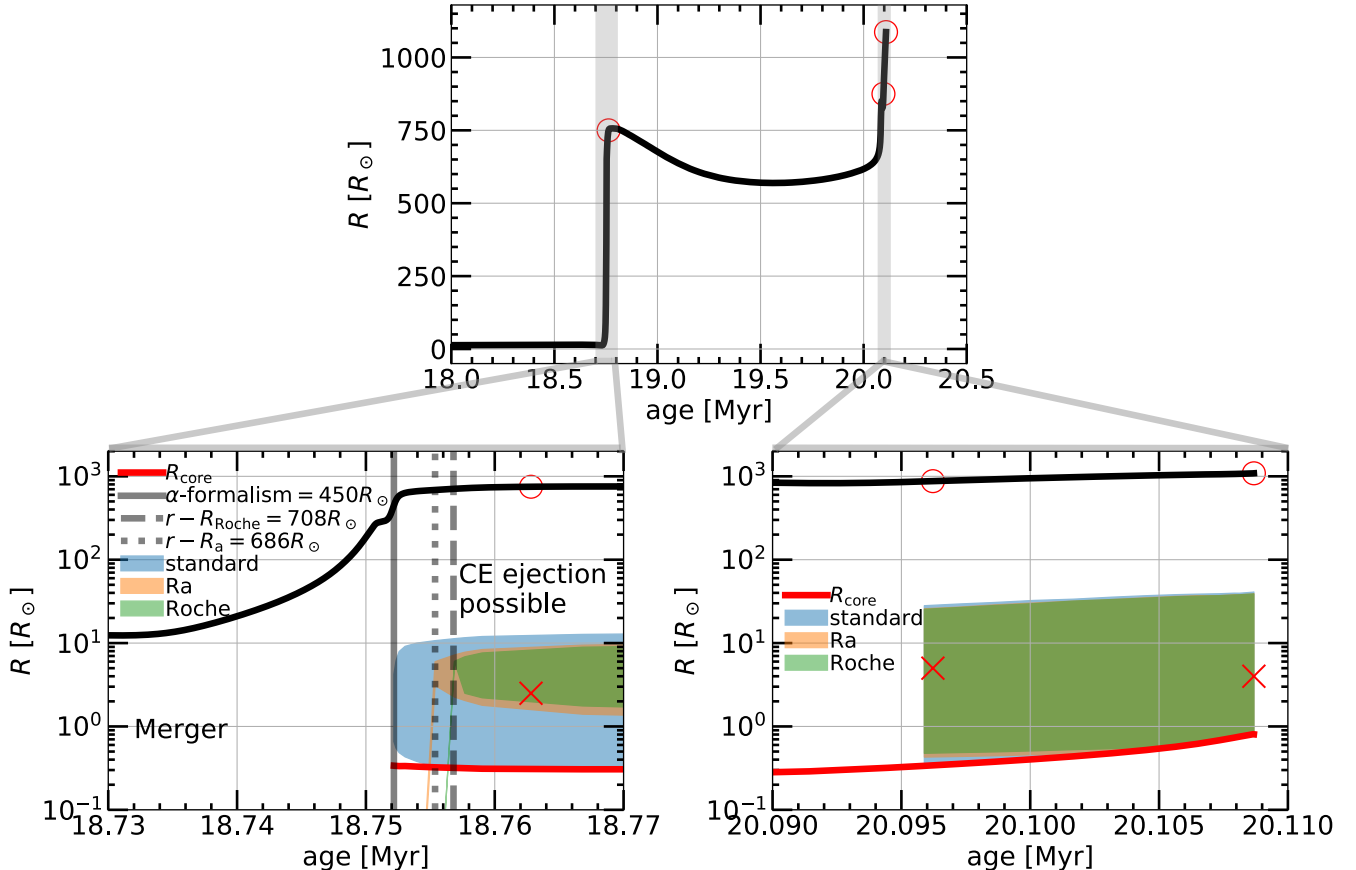
3. RESULTS

3.1. *1D modeling*

Figure 1. MESA evolutionary history for the $12M_\odot$ primary (donor) star. Top: radius vs. time. Red circles indicate the models we simulate in 3D hydrodynamics. Bottom left: focus on the first rise (expansion). Vertical lines indicate the earliest ages where CE ejection is possible and shaded regions indicate the radius ranges where CE ejection is possible according to our adjusted 1D energy formalism. Red line indicates the radius of the He core. Red 'X's indicate final orbital separation from our 3D hydrodynamics simulations. Bottom right: focus on the second rise. See §C for further details on the MESA model.

The top panel of Figure 1 shows radius vs. time for the initially $12M_\odot$ donor, evolved as a single star using the setup of Götberg et al. (2018). The red circles indicate the three different initial conditions we simulate in 3D hydrodynamics: near the first peak ($R_\star = 750R_\odot$, $M_\star = 11.8M_\odot$), on the second rise ($R_\star = 900R_\odot$, $M_\star = 9.9M_\odot$), and at the second peak ($R_\star = 1080R_\odot$, $M_\star = 9.8M_\odot$). The first peak corresponds to RLOF (Roche-lobe overflow) during late hydrogen-shell burning (case B; e.g., Kippenhahn & Weigert 1967) and the second peak to RLOF after core-helium burning (case C; e.g., Lauterborn 1970). In all three cases, the donor has a deep convective envelope and the mass transfer is dynamically unstable.

In the bottom panels, we zoom in on the first and second rises (expansions). The radius of the He core is shown in red (defined by the `he_core_mass` attribute in MESA, using `he_core_boundary_h1_fraction ≥ 0.01` and `min_boundary_fraction ≥ 0.1`). It is $R_{\rm core} = 0.31R_\odot$ for the first peak, $R_{\rm core} = 0.36R_\odot$ for the sec-

ond rise, and $R_{\rm core} = 0.8R_\odot$ for the second peak. For a given stellar age, the predicted radius ranges where CE ejection is possible as predicted by the three 1D energy formalisms (standard α formalism, $r - R_a$ adjusted formalism, and $r - R_{\rm Roche}$ adjusted formalism) are shown in shaded blue, orange, and green respectively (see §2.2). We start the FLASH simulations just within these ranges (see §2). Red 'X's indicate the time at which the envelope is ejected in our 3D hydrodynamics simulations (see Figure 4).

The bottom left panel focuses on the first rise. The earliest ages at which CE ejection is possible from the 1D energy formalisms are indicated by the vertical lines. The bottom right panel focuses on the second rise. Here the different energy formalisms predict a similar range of radii for possible CE ejection, and in the 3D hydrodynamics we eject the envelope within these ranges.

We calculate the minimum radius on the second rise in which Roche-lobe overflow is possible, accounting for orbital widening of the binary as a result of mass loss

by fast stellar winds during its prior evolution (see §E for discussion and details on this). We find that after the first peak (at $R_\star = 757 R_\odot$), for radii less than $R_\star = 900 R_\odot$ on the second rise, RLOF will not occur. Thus, we simulate three models in 3D hydrodynamics that are chosen to span the range of stellar structures in which dynamical CE ejection is possible for a $12 M_\odot$ primary: near the first peak ($R_\star = 750 R_\odot$), on the second rise ($R_\star = 900 R_\odot$), and at the second peak ($R_\star = 1080 R_\odot$). We note that the $750 R_\odot$ and $1080 R_\odot$ models may appear fine-tuned in isolation, but they are chosen so that our suite of 3D hydrodynamics simulations in this paper span the parameter space of stellar structures that will lead to dynamical CE ejection.

3.2. 3D hydrodynamics

Figure 2 shows 3D volume renderings of three fields (density, velocity, and energy) at three times: early in the evolution (11 hr), at an intermediate time (16 hr), and at a relatively late time (25 hr) when the envelope has just been ejected. We show renderings for the $900 R_\odot, v_i = v_{\rm circ}$ (circular initial velocity) simulation. Results are qualitatively similar for all of the other simulations. The volume renderings are of the bottom half of the orbital plane ($z < 0$, with $J_{\rm orb} \parallel z$), with a color map and transfer function chosen to highlight the dynamic range and structure of the field being studied. See §A for the detailed time evolution of these three fields and a zoom-in on the core.

The 1st row of Figure 2 shows the logarithm of gas density. In the first panel, one can see the density shells that are progressively disturbed as the secondary sweeps through the primary's envelope. At late times, the structure is quite disturbed and resembles a differentially rotating disk, though at even later times, the secondary stalls and "parks" at its final orbital separation (see Figure 3).

The 2nd row of Figure 2 shows the ratio of absolute magnitude of velocity to the local escape velocity for each cell, $|v|/v_{\rm esc,local}$. Pink corresponds to gas that is bound to the system (values < 1) and green corresponds to gas that is not bound to the system (values > 1). The blue isosurface is at $|v|/v_{\rm esc,local} = 1$. At late times (after a few orbits of the secondary), nearly all of the envelope is at $|v| > v_{\rm esc,local}$ and is gravitationally unbound from the star. Some of the envelope material is shocked to $|v| \gtrsim 6 v_{\rm esc,local}$ on the leading edge of a spherically expanding shell. One can see the envelope being shocked and swept preferentially outwards as the secondary orbits the center of mass of the primary. As the secondary moves through the envelope of the primary, it acts as a local diffusive source term, giving surrounding mate-

rial roughly outward velocities. We also analyzed the velocity vectors of each grid cell, and found that they are nearly all pointed outwards from the core as a result of the secondary's repeated passages, ejecting the envelope.

The 3rd row of Figure 2 shows specific energy (the sum of specific kinetic and potential energy, internal energy is not included). Pink-purple corresponds to bound ($\varepsilon < 0$) and yellow corresponds to unbound ($\varepsilon > 0$). There is a blue isosurface at $\varepsilon = 0$. At early times, the binding energy of most cells is negative. At late times, nearly all of the material in the box (except for the surviving core) has positive energy. The core and secondary have separate Roche lobes, and the equipotential surface of $\varepsilon = 0$ (blue isosurface) is confined to a small region around the core. The size of this region decreases with time and number of orbits until the secondary stalls at its final orbital separation. This qualitatively shows complete envelope ejection.

In the bottom left panel of Figure 2 one can see a crescent-shaped sliver of material on the left hand side of the panel that becomes unbound.

This is due to the change in the mass distribution interior to the radius of this sliver (initially at $r \approx 10 R_\odot$) caused by the secondary sweeping out mass on the right hand side. The gravitational potential due to the enclosed mass changes and this sliver of material becomes unbound due to gravitational effects (acting nearly instantaneously) as opposed to hydrodynamical effects (acting on the dynamical time).

We now discuss the orbital parameters of the two objects and in particular the secondary as it orbits the center of mass of the primary donor star. The left panel of Figure 3 shows the trajectory of the center of mass of the primary and the secondary as a function of time in two of our simulation box coordinates (x and y; because our simulation is symmetric along the z-axis, there is little evolution of the center of masses in z). We show the evolution for the two $900 R_\odot$ simulations, with $v_i = v_{\rm circ}$ and $v_i = v_{\rm integrator}$, where $v_{\rm integrator}$ is the initial velocity vector informed by the 2D kinematics study. Blue and green 'X's mark the time at which the envelope is ejected (see Figure 4).

The right panels of Figure 3 show the separation $a(t)$ between the center of mass of the primary and the position of the point mass secondary vs. time for the same two simulations. Results for our other simulations are qualitatively similar. The final orbital separations and the energies as a function of time for all simulations are shown in Figure 1 and Figure 4 respectively. Several "bounces" are observed as the secondary orbits the core.
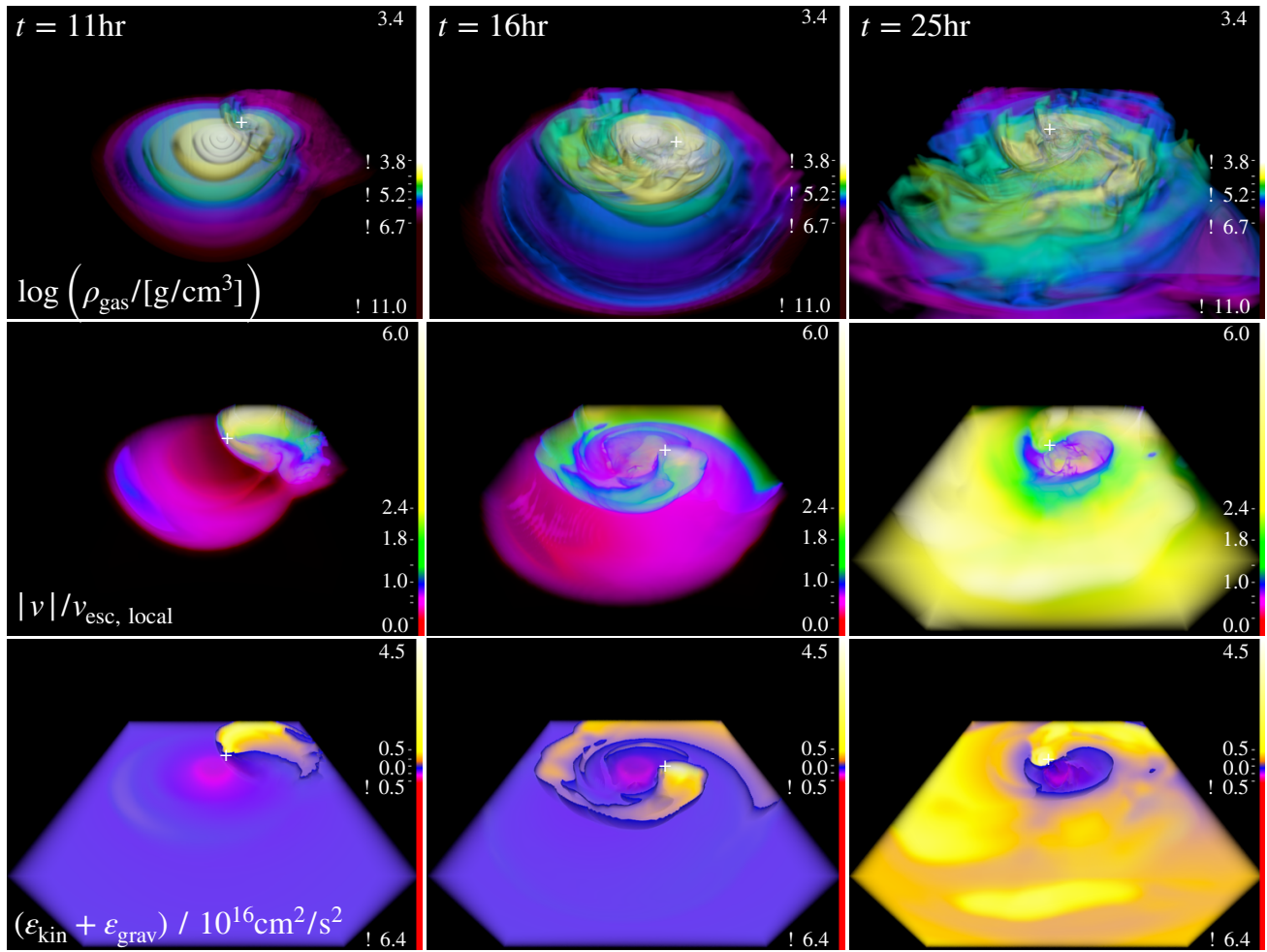
Figure 2. 3D renderings of three fields (density, velocity, and energy) at three times: early in the evolution (11 hr), at an intermediate time (16 hr), and at a moderately late time (25 hr) when the envelope has just been ejected. We show the $900R_\odot, v_i = v_{\rm circ}$ simulation; results are qualitatively similar for all our other simulations. 1st row: logarithm of gas density. Shells corresponds to different density isosurfaces. 2nd row: ratio of velocity magnitude to local escape velocity, $|v|/v_{\rm esc,local}$. Blue isosurface is at $|v|/v_{\rm esc,local} = 1$, pink-red is < 1, green-yellow is > 1. 3rd row: sum of specific kinetic and potential energy. Blue isosurface at $\varepsilon = 0$, pink-purple corresponds to bound ($\varepsilon < 0$) and yellow corresponds to unbound ($\varepsilon > 0$). White '+' indicates position of secondary. Videos available at https://youtube.com/channel/UCShahcfGrj5dOZTTrOEqSOA.

The initial velocity vector informed by the 2D kinematics (see Section 2) occurs near the pericenter of an eccentrically inspiraling orbit and it is thus higher energy (larger velocity) than the circular initial velocity. The run using this vector stalls and "parks" at an orbital separation of $a_{\rm f} \approx 2.8R_\odot$. The circular initial velocity simulation parks at an orbital separation of $a_{\rm f} \approx 1.2R_\odot$. For reference, the final orbital separation of the $750R_\odot$ simulation is $a_{\rm f} \approx 1.1R_\odot$ and the final orbital separation of the $1080R_\odot$ simulation is $a_{\rm f} \approx 1.4R_\odot$. After supernova kicks (calculated with 1000 randomly oriented kicks and a nominal kick magnitude of 250 km/s; Hobbs et al. 2005), we calculate that these systems will form binary neutron stars that merge within 0.01–1 Gyr (95% confidence interval of the probability distribution). See §F for details of this calculation.

We estimate the $\alpha_{\rm CE}$-equivalent efficiency, where $\alpha = E_{\rm bind,env}/\Delta E_{\rm orb} \approx 2a_{\rm f}E_{\rm bind}/(GM_{\rm core}M_{\rm secondary})$. For the $R_\star = 900R_\odot$ run, taking $a_f = 2.8R_\odot$, $M_{\rm core} = 4.5M_\odot$, $M_{\rm secondary} = 1.4M_\odot$, $M_{\rm donor} = 9.9M_\odot$, and $a_i \approx 1000R_\odot$, using Eq. 1 we find $\Delta E_{\rm orb} \approx 4.2 \times 10^{48}$ erg. The binding energy at $2.8R_\odot$ is (see Figure 11) $E_{\rm bind} \approx 5.5 \times 10^{47}$ erg. This gives an $\alpha_{\rm CE}$-equivalent efficiency of $\alpha_{\rm CE} \approx 0.13$. Similarly, for the $R_\star = 750R_\odot$ run, taking $a_f = 1.1R_\odot$, we find $\alpha_{\rm CE} \approx 0.38$. For the $R_\star = 1080R_\odot$ run, taking $a_f = 1.4R_\odot$, we find $\alpha_{\rm CE} \approx 0.08$. Thus, the $\alpha_{\rm CE}$ is small for the models we study, but we note that this may be specific for these extended progenitors.

In comparison, based on their final orbital separation, the 1D MESA study of Fragos et al. (2019) (who studied a different primary model; see Figure 10) find a high
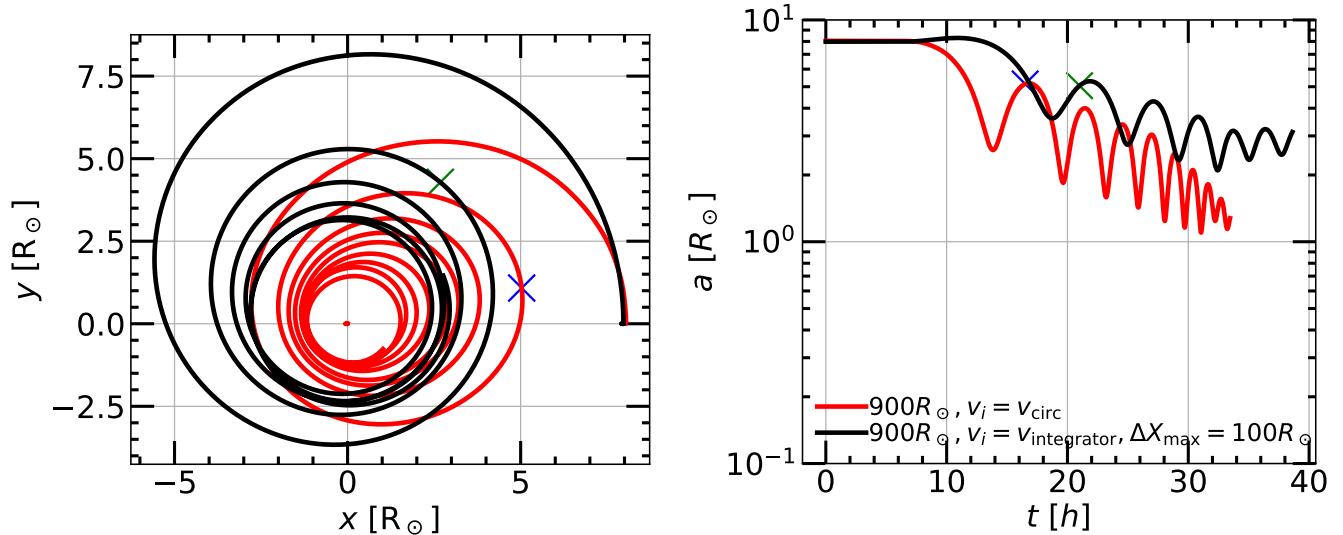
Figure 3. Trajectory and orbital separation for two $900R_\odot$ simulations with different initial velocities. Black is $900R_\odot, v_i = v_{\mathrm{integrator}}, \Delta X_{\mathrm{max}} = 100R_\odot$, red is $900R_\odot, v_i = v_{\mathrm{circ}}$. Blue and green 'X's mark the time at which the envelope is ejected for the v_{circ} and $v_{\mathrm{integrator}}$ runs respectively (see Figure 4). Left: trajectory. Black/red line is secondary (NS), red dot is center of mass of primary (donor star). Right: separation $a(t)$ between center of mass of primary and position of point mass secondary vs. time.

α_{CE}-equivalent efficiency of ≈ 5, though we note that this study finds envelope ejection in the self-regulated regime and α_{CE} is calculated after a mass-transfer phase which occurs after the envelope is ejected. After envelope ejection, in our simulations, we expect a stable mass transfer phase to occur between the surviving core and the NS (as in Fragos et al. 2019), which will further alter the separation before the supernova takes place.

We now turn to a calculation of the energy of each cell in the simulation box as a function of time. Figure 4 shows specific energy ($\varepsilon = \varepsilon_{\mathrm{kin}} + \varepsilon_{\mathrm{grav}}$) vs. time, for material outside of the current orbit of the secondary (see Figure 3) for all of the models we simulate in 3D hydrodynamics. We note that the recombination energy, while not included in our simulations, is small compared to the binding energy of the envelope here; for hydrogen, $\varepsilon_{\mathrm{recomb}} \approx 13.6$ eV$/m_{\mathrm{p}} \approx 10^{19}$ erg/g, whereas the envelope energy is $\varepsilon \approx 10^{21}$ erg/g (Figure 4). The energy of this material increases with time, transitioning from negative (bound) to positive (unbound) at $t \approx 15$–20 h. Small-scale variations correspond to the "bounces" in orbital separation as a function of time with each successive orbit of the secondary (Figure 3).

We successfully eject the envelope for all of our simulated models, which span the range of stellar age and radii in which dynamical CE ejection is predicted to be possible for an initially $12M_\odot$ primary. We note that we do not include internal or recombination energy in calculation of the envelope energy (which some contemporary studies do, and which is a positive quantity that helps

with envelope ejection), only kinetic and gravitational potential energy. As a second verification of envelope ejection, we also calculate the mass ejected (unbound) from the primary as a function of time. We find that the secondary ejects the entire mass of the envelope (including all of the hydrogen; see below).

The mass enclosed inside the orbit of the secondary does not change appreciably over the course of the simulation; we verify that mass does not "leak" significantly from the inner regions of the star due to numerical effects (see §G). Thus, we estimate that the inspiral is not driven by the increased numerical drag due to the core mass leaking out towards the secondary (because none of this leaked mass reaches the secondary's orbit) but is instead driven by regular numerical drag due to the 3D hydrodynamical grid that is a resolution-dependent effect (see §G for our numerical convergence study).

We now briefly discuss the chemical abundance of the ejecta. Figures 5 shows 3D renderings of the mass fraction of hydrogen, helium, and nitrogen, at three times for the ($900R_\odot, v_i = v_{\mathrm{circ}}$) run. Results for other runs are qualitatively similar. Though it contributes significantly to the total mass fraction, we did not include a rendering of carbon as the carbon remains relatively sequestered near the core rather than mixing with the outer debris as the hydrogen, helium, and nitrogen do. See §C for 1D composition profiles of these elements at the beginning of the simulation. All composition data is available upon request.
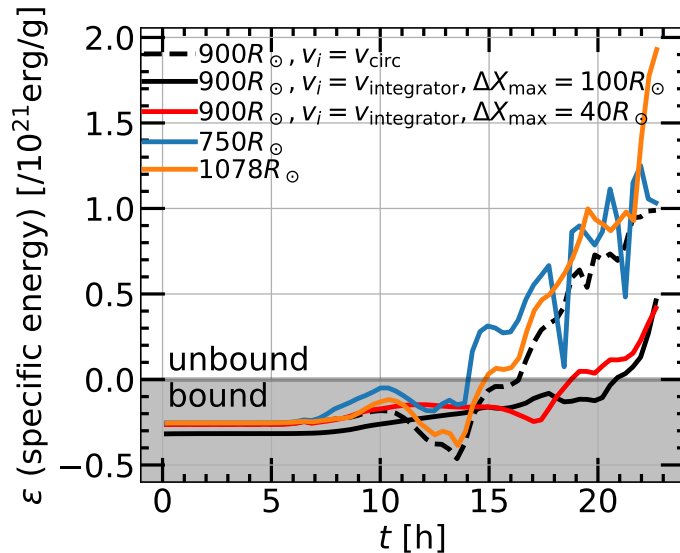
3.3. *Recombination Transient*

Figure 4. Sum of specific kinetic and potential energy ($\varepsilon = \varepsilon_{\mathrm{kin}} + \varepsilon_{\mathrm{grav}}$) vs. time for material outside of the current orbit of the secondary (see Figure 3) for all simulations. Envelope is bound for $\varepsilon < 0$ (grey region) and envelope is ejected for $\varepsilon > 0$.

The most notable result is that the hydrogen envelope is completely ejected at late times; this implies no hydrogen will be visible in the spectrum of the surviving stripped star as the surface hydrogen mass fraction is nearly zero. The expanding hydrogen bubble is observable as a hydrogen recombination transient Ivanova et al. (2013a). We use Eqns. (A1), (A2), and (A3) of MacLeod et al. (2017b), based on Ivanova et al. (2013a)'s application of the analytic theory of recombination transients (e.g., Popov 1993; Kasen & Woosley 2009; Kasen & Ramirez-Ruiz 2010) to estimate the luminosity, timescale, and total energy of this recombination transient (see §B for details of the calculation). Using $R_{\mathrm{init}} \approx 2R_\odot$ (approximate stalling orbital separation of the secondary across our models), $\Delta M \approx 5M_\odot$ (the entire mass of the envelope), $v_{\mathrm{ej}} \approx 18$ km/s (the velocity at $10R_\odot$ at the end of our simulation), $\kappa \approx 0.32$ cm^2 g, and $T_{\mathrm{rec}} \approx 4500$ K, we find $L_{\mathrm{p}} \approx 10^{37}$ erg s^{-1}, $t_{\mathrm{p}} \approx 274$ d, and $E_{\mathrm{rad,p}} \approx 2 \times 10^{44}$ erg. The mass of the stripped star is $M_\star \approx 4.5M_\odot$, radius $R_\star \approx 1R_\odot$. We note a stripped star and neutron star are also interesting as a "living" gravitational wave source potentially observable with LISA (Götberg et al. 2020). See §4 for discussion on extensions to our framework to study the remnant in more detail and for longer timescales.

Roughly 10% of the brightest luminous red novae (LRN) transients, which have been previously associated with stellar mergers and common-envelope ejections, are predicted to occur at some point in binary neutron star forming systems (Howitt et al. 2020; Vigna-Gómez et al. 2020). LRN have come to be associated with stellar mergers through detailed study of a few

landmark events. M31 RV was one of the first LRN to be identified, in 1988, but the light curve of the transient is only captured during the decline (e.g., Mould et al. 1990). The galactic transient V1309 Sco proved essential in establishing the nature of these events as stellar mergers (Mason et al. 2010; Nicholls et al. 2013). Noteworthy transients arising from a relatively massive stars include M31LRN 2015 with a progenitor of $M_\star \approx$ 3–5.5$M_\odot$ (MacLeod et al. 2017b) and M101 OT2015-1 with a progenitor of $M_\star \approx 18M_\odot$ (Blagorodnova et al. 2017).

4. DISCUSSION

Here we briefly compare to other work, discuss uncertainties in the 1D stellar modeling, resolution-dependent effects in the 3D hydrodynamics, and comment on future work.

4.1. *Comparison to other work*

We briefly compare to other work below, though we note that no other 3D hydrodynamics simulations have been conducted to simulate CE ejection leading to a binary neutron star system, thus with our mass ratios (which are more extreme than the current literature) or stellar radii (which are also relatively larger than the current literature). The main difference with these works, besides the star studied, is that the initial conditions of our 3D hydrodynamics simulations are informed using an adjusted 1D energy formalism (see §2) and a 2D kinematics study.

There has been five decades of work on the CE phase (see e.g., Ivanova et al. 2013b), and there is an extensive
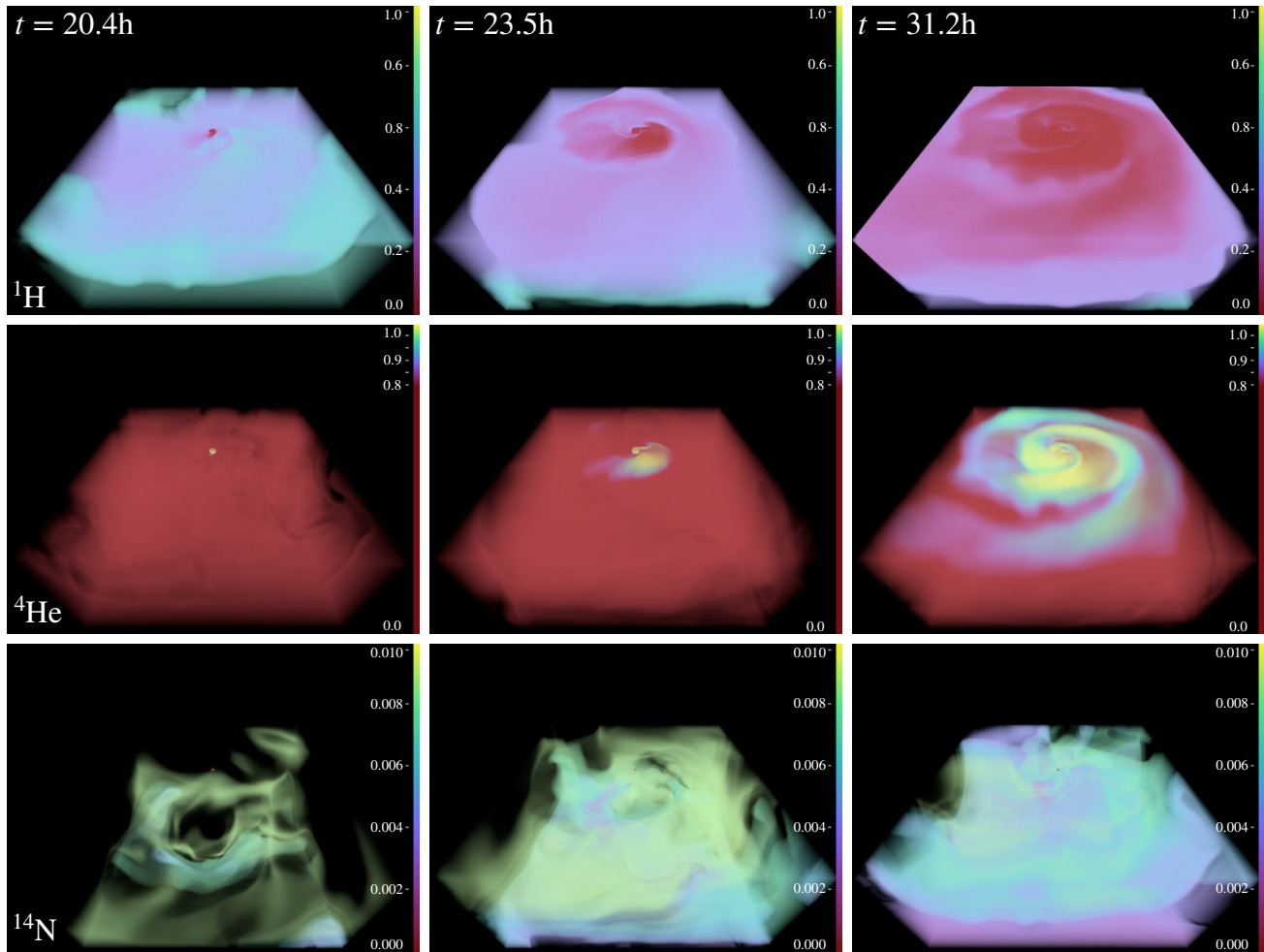
Figure 5. 3D renderings of mass fraction of hydrogen, helium, and nitrogen as a function of time, for the $(900R_\odot, v_i = v_{\text{circ}})$ run. Results for other simulations are qualitatively similar. The colormap is the same for each element but note that the scale changes for each element in order to highlight the structure. For hydrogen and helium, mass fractions range from 0 (dark purple) to 1 (light yellow). For nitrogen, mass fractions range from 0 (dark purple) to 0.01 (light yellow).

literature on CE ejection (we review some below); however, the most relevant comparison for our work is to the 1D study of Fragos et al. (2019), who also study BNS formation through the CE phase. These authors study a different (though comparable) MESA model to ours (see Figure 10) and thus a direct comparison is not possible. We note our 1D formalism predicts that the model studied by Fragos et al. (2019) is in a boundary region where the outcome of CE evolution is unclear. The authors find CE ejection in the self-regulated regime. We study CE ejection in the dynamical regime, and find that for all of the models we simulate in 3D hydrodynamics, the envelope is ejected in the dynamical regime. Fragos et al. (2019) find a final orbital separation of $a_f \approx 3.3$–$5.7R_\odot$. We find final orbital separations of $a_f \approx 1.1$–$2.8R_\odot$. While it is valuable to model the CE evolution from start to finish, the 1D treatment that is necessary to facilitate this has inherent limitations. For example,

Fragos et al. (2019) assume complete and instantaneous spherically symmetric sharing of orbital energy with the envelope. This is an nonphysical assumption that can only be addressed by 3D hydrodynamics.

Results from other studies of CE ejection for lower mass ratio systems are listed below. Generally, contemporary studies have been unable to eject the envelope in the course of the 3D simulation. The fact that we are able to successfully and robustly eject the envelope, without including internal or recombination energy (which is claimed to be essential to CE ejection in some contemporary work at lower masses; see below), is likely due to the fact that we study an evolved $12M_\odot$ red supergiant primary; thus, the secondary encounters a very different density profile during its inspiral that the density profiles in the works listed below. Sandquist et al. (1998) find 23-31% envelope ejection in simulations with $3M_\odot$ and $5M_\odot$ AGB primaries. Staff et al. (2016) find

25% envelope ejection with a $3.05M_\odot$ ($3.5M_\odot$ ZAMS mass) AGB primary. Sand et al. (2020) find <20% envelope ejection when not accounting for recombination energy, and complete envelope ejection when including recombination energy, for a $1M_\odot$, $174R_\odot$ early-AGB star with companions of different masses. Chamandy et al. (2020) find an envelope unbinding rate of 0.1–$0.2M_\odot$ yr, implying envelope unbinding in <10 yr, for a $1.8M_\odot$, $122R_\odot$ AGB primary with $1M_\odot$ secondary.

We note that many contemporary studies that attempt to simulate systems in which one star is highly centrally concentrated have replaced the core of that star with a point mass, and the core's density profile with a much less centrally-concentrated polytrope. This shortcut creates an artificial boundary and makes it easier to eject the envelope. In this work we fully resolve the core of the star, allowing for a realistic treatment of the inspiral and material interior to the secondary's location as it stalls and "parks" at a final orbital separation.

4.2. *Uncertainties due to prior evolution*

There are four main disclaimers to our analysis, and indeed to our initial stellar models in general:

First, our model of the $12M_\odot$ donor was evolved as a single star. However, for the progenitor system of a BNS merger, the typical scenario includes a stable mass transfer phase before the formation of the NS (e.g., Tauris et al. 2017). Therefore, the donor star at the CE phase is the initially less massive star which has possibly accreted mass from the NS progenitor and survived the passage of the supernova shock. While the latter has only a moderate effect on the stellar structure (e.g., Hirai et al. 2018), the phase of stable mass transfer can lead to high rotation (e.g., Hut 1981; Cantiello et al. 2007; de Mink et al. 2013), chemical pollution with He (e.g., Blaauw 1993), and mixing of fresh hydrogen in the core. These effects can influence the stellar radius significantly (e.g., rotation can increase the equatorial radius, He-richness can contribute to keep the star more compact), and most importantly change the density profile just outside the core (i.e., in the domain of our 3D simulation) with the rejuvenation-inducing mixing. A second order effect is the impact on the wind mass loss rate (and thus orbital evolution) of the system (e.g., Renzo et al. 2017). While these require further investigation, our models provide a proof-of-concept of our methods that could be applied to more realistic post-RLOF CE donors.

Second, we do not accurately know the distribution of separations that systems have at the time when star one is a neutron star and the other star is a red supergiant.

Third, in considering the orbital evolution prior to filling the Roche lobe, we use the Jeans approximation for widening as a result of stellar wind mass loss (see §E). The Jeans approximation may not actually hold for the donor star. The mass loss occurs in the late phases and the systems of interest in this work will be very close to Roche-lobe filling at this stage. We may have wind focusing (e.g., Mohamed & Podsiadlowski 2007). It is possible that the systems shrink instead of widening. In that case, the forbidden region (see §E) might no longer be forbidden.

Fourth, our results depend on how accurate our progenitor models are. These are subject to all of the uncertainties that affect massive star evolution, most notably those related to mass loss (e.g., Renzo et al. 2017) and internal mixing (e.g., Davis et al. 2019). These affect the final structure and core mass at the moment of Roche-lobe filling.

4.3. *Numerical resolution*

Our resolution is sufficient to achieve common envelope ejection and stall/"park" at a final orbital separation of $a_{\rm f} \approx 1.1$–$2.8R_\odot$ in our simulations. However, there is mass leakage and redistribution from the highly centrally concentrated core ($\rho_c \approx 10^3$–10^6 g/cm^3) at radii $R < 0.3R_\odot$ (see Section G). Because it occurs at radii significantly smaller than the position of the secondary, this redistribution of mass should not have an effect on the secondary's orbit (Gauss' theorem). The largest numerical effect on the secondary's orbit is the numerical diffusion introduced by the grid (as in any 3D hydrodynamics simulation). This effect decreases with increasing resolution. We discuss this further in Section G.

Our FLASH setup uses a cartesian grid, which does not conserve angular momentum L (this happens any time there is rotational motion across a grid cell). This causes the point mass to inspiral more rapidly. This is in comparison to explicitly Galilean-invariant codes such as moving-mesh codes. For example, Ohlmann et al. (2016) quote that L was conserved during their run with an error below 1%. Technically, our FLASH setup violates Galilean invariance, as do other conventional grid-based hydrodynamics codes (when altering the background velocity at the same resolution), but as Robertson et al. (2010) showed, this is a resolution-dependent effect, and L in grid codes approaches perfect conservation at very high resolutions. The non-conservation of L becomes larger with each orbit (the longer the simulation is run). Thus, if we have successful CE ejection, which we do, this likely represents a "lower limit" of possible CE ejection, because with perfect conservation of L the point

mass would orbit more times and have longer to strip and eject the CE. While our detailed results are somewhat resolution-dependent to a certain extent (though not significantly; see §G), the main result of this work—successful CE ejection leading to binary neutron star formation for all of the models we study—is robust and will only become stronger at higher resolutions.

4.4. *Future work*

The framework developed in this work can be used to study various binary stellar phenomena. First, we can study the large parameter space of systems that can be accurately modeled as a star–point mass interaction, including different mass ratios, primary/donor stars, and metallicities. We plan to perform a parameter-space study of CE systems leading the binary neutron stars and black hole/neutron star binaries. We also plan to study the long-term evolution by exporting the FLASH simulation back to MESA (this capability was already explored in Wu et al. 2020).

The astrophysical context provided by a detailed physical understanding of the CE phase allows one to use GW and EM observations of binary neutron star mergers as tools to answer a broader set of questions than the raw GW data alone can answer, for example, on the lives and deaths of stars, the difficult-to-probe physics of the deep interiors of stars, and how nucleosynthesis operates in the Universe.

In another direction, we can adjust our framework to follow the ejected material in more detail to inform our understanding of supernovae that interact with material from CE ejections. This may also help to understand some stars in the Galaxy that have interacted with CE material.

In the longer term, we plan to extend our FLASH setup to initialize two separate MESA stars. This would (in theory) allow us to study the entire parameter space of star-star interactions, leading to both stellar mergers and CE ejections.

5. CONCLUSION

The main points of this paper are summarized below.

1. We study the dynamical common envelope evolution of an initially $12M_\odot$ red supergiant star and a $1.4M_\odot$ neutron star in 3D hydrodynamics.

2. Most earlier studies have focused on low mass stars. This is the first successful 3D hydrodynamics simulation of a high mass progenitor that results in a binary neutron star that merges within a Hubble time.

3. We fully resolve the core of the star to $\lesssim 0.005R_\odot$ and our 3D hydrodynamics simulations are informed by an adjusted 1D analytic energy formalism and a 2D kinematics study.

4. We study different initial separations where the donor fills its Roche lobe during the first ascent of the giant branch and after the completion of central helium burning.

5. We find complete envelope ejection (without requiring any other energy sources than kinetic and gravitational energy) during the dynamical inspiral for all of the models we study.

6. We find a final orbital separation of $a_f \approx 1.1$–$2.8R_\odot$ (before any supernova kick) for the models we study, which span the range of initial separations in which dynamical CE ejection is possible for a $12M_\odot$ star. These systems will form binary neutron stars that will merge within 0.01–1 Gyr. We find an α_{CE}-equivalent efficiency of ≈ 0.1–0.4 for the models we study, but this may be specific for these extended progenitors.

7. The framework developed in this work can be used successfully to study the diversity of common envelope progenitors in 3D hydrodynamics.

APPENDIX

A. DETAILED TIME EVOLUTION

Here we show the evolution during the neutron star's inspiral for the $(900R_\odot, v_i = v_{\text{integrator}})$ run. See Figure 3 for the trajectory and orbital separation as a function of time (black line). The animated video Figure 7 shows a 3D rendering of the material near the core of the primary, from initial inspiral through common envelope ejection and stalling ("parking") of the neutron star at its final orbital separation. Different shells corresponds to different density isosurfaces. While the material inside the core of the primary remains relatively undisturbed (as the closest approach of the secondary is $r \approx 2R_\odot$ and the radius of the core is $R_{\text{core}} \approx 0.35R_\odot$), the material outside the core (both interior to and exterior to the orbit of the neutron star) is swept away and cleared with each successive passage of the neutron star. Red '+' (or '→' if it is outside the domain) indicates the position of the neutron star. It is apparent that the neutron star is able to effectively clear the material interior to its orbit but outside the core (in addition to ejecting the envelope), allowing it to "park" at a final orbital separation (for this simulation) of $a_{\text{f}} \approx 2.8R_\odot$.

The animated video Figure 7 shows a 3D rendering of the material for the entire domain, as opposed to a zoom-in on the material near the core in Figure 6. While in Figure 6 we saw that the core remained relatively undisturbed and that there was not significantly more material in between the orbit of the neutron star and the core, here the focus is the severely disturbed material in the envelope. One can see the "spiral-wave" feature as the neutron star sweeps out envelope mass with each successive passage in its orbit. One can also see that some of the higher density material closer to the core is moved outward toward the periphery as the neutron star ejects this material.

The animated video Figure 8 shows a 3D rendering of the ratio of the velocity magnitude to the local escape velocity, $|v|/v_{\text{esc,local}}$ as a function of time. As the neutron star orbits the center of mass of the red supergiant star, it strips off the envelope material outside its orbit, unbinding it and shocking this material to velocities in excess of $6v_{\text{esc,local}}$. These large velocities are an indication of how efficiently the orbital energy of the neutron star is transferred to the energy of the envelope.

The animated video Figure 9 shows a 3D rendering of the sum of the specific kinetic and potential energy as a function of time. There is a blue isosurface at $\varepsilon = 0$, pink-purple corresponds to bound material ($\varepsilon < 0$), and yellow corresponds to unbound material ($\varepsilon > 0$). As in Figure 8, the envelope gains more energy with each orbital passage of the neutron star and becomes progressively more unbound (the colors become a brighter yellow with time).

B. HYDROGEN RECOMBINATION TRANSIENT

Here we outline the details of our estimate of the properties of the hydrogen recombination transient from the ejected hydrogen envelope (see §3). We use Eqns. (A1), (A2), and (A3) of MacLeod et al. (2017b), based on Ivanova et al. (2013a)'s application of the analytic theory of recombination transients (e.g., Popov 1993; Kasen & Woosley 2009; Kasen & Ramirez-Ruiz 2010) to estimate the luminosity, timescale, and total energy of the hydrogen recombination transient predicted by our 3D hydrodynamics simulations:

$$L_{\text{p}} \approx 4.2 \times 10^{37} \text{ erg s}^{-1} \left(\frac{R_{\text{init}}}{10R_\odot}\right)^{2/3} \left(\frac{\Delta M}{0.1M_\odot}\right)^{1/3} \left(\frac{v_{\text{ej}}}{100 \text{ km s}^{-1}}\right)^{5/3} \left(\frac{\kappa}{0.32 \text{ cm}^2 \text{ g}^{-1}}\right)^{-1/3} \left(\frac{T_{\text{rec}}}{4500 \text{ K}}\right)^{4/3}, \quad \text{(B1)}$$
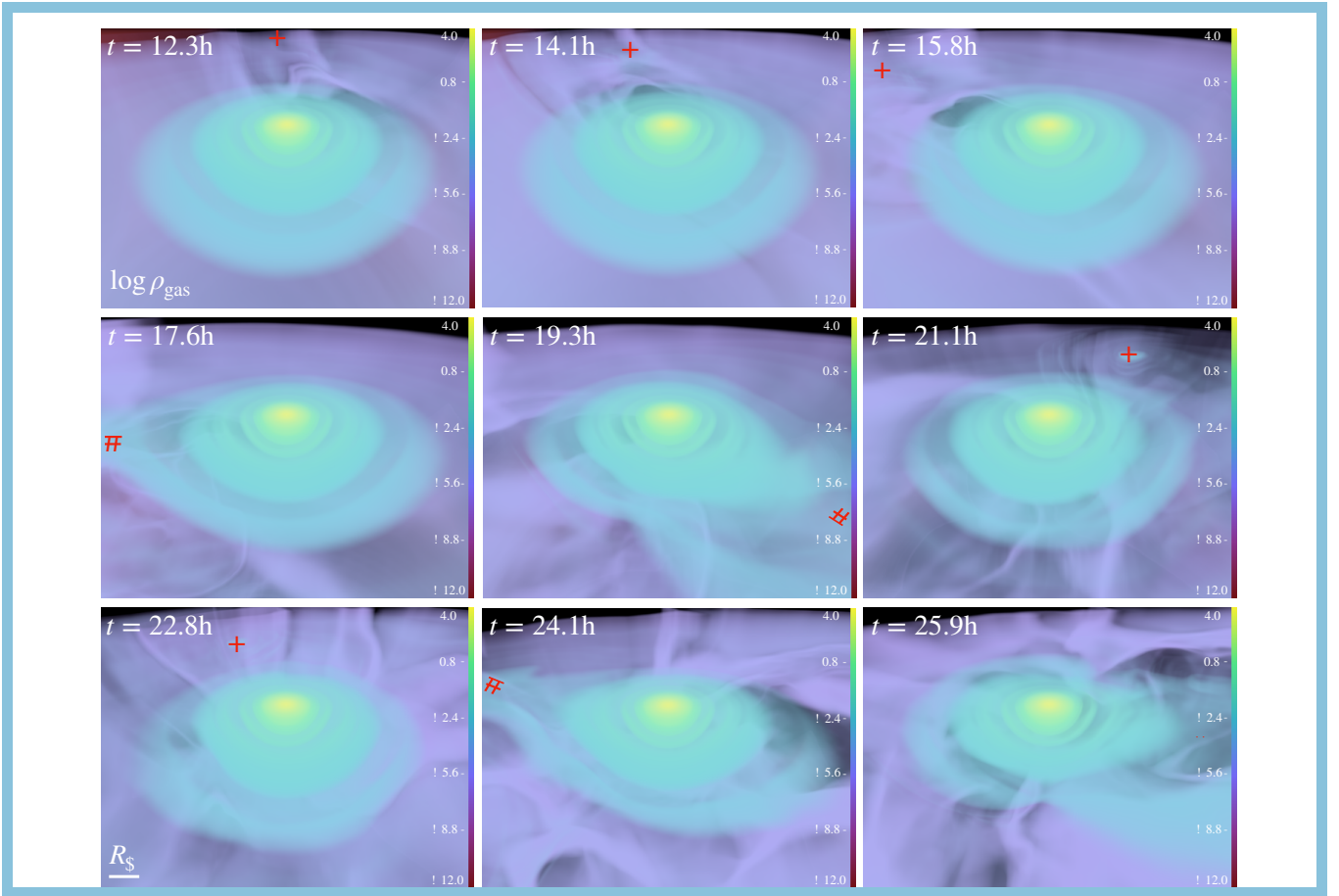
$$t_{\text{p}} \approx 42 \text{ d} \left(\frac{R_{\text{init}}}{10R_\odot}\right)^{1/6} \left(\frac{\Delta M}{0.1M_\odot}\right)^{1/3} \left(\frac{v_{\text{ej}}}{100 \text{ km s}^{-1}}\right)^{-1/3} \left(\frac{\kappa}{0.32 \text{ cm}^2 \text{ g}^{-1}}\right)^{1/6} \left(\frac{T_{\text{rec}}}{4500 \text{ K}}\right)^{-2/3}, \quad \text{(B2)}$$

$$E_{\text{rad,p}} \approx 1.5 \times 10^{44} \text{erg} \left(\frac{R_{\text{init}}}{10R_\odot}\right)^{5/6} \left(\frac{\Delta M}{0.1M_\odot}\right)^{2/3} \left(\frac{v_{\text{ej}}}{100 \text{ km s}^{-1}}\right)^{4/3} \left(\frac{\kappa}{0.32 \text{ cm}^2 \text{ g}^{-1}}\right)^{-1/6} \left(\frac{T_{\text{rec}}}{4500 \text{ K}}\right)^{2/3}. \quad \text{(B3)}$$

Figure 6. Video figure (viewable online). Video shows a 3D rendering of the logarithm of gas density ($[\mathrm{g/cm^3}]$) for material near the core of the primary (the domain is of the video here is $x \approx 10R_\odot$ on a side) during the neutron star's inspiral for the ($900R_\odot$, $v_i = v_{\mathrm{integrator}}$) run. Shells correspond to different density isosurfaces; white is highest density, dark purple is lowest density. Video shows that the neutron star significantly disturbs the density structure of the envelope as it orbits and "stalls" at a final orbital separation, but that the core of the star remains largely undisturbed. Position of the neutron star is indicated by the red '+', or '→' if it is outside the domain. Videos also available at https://youtube.com/channel/UCShahcfGrj5dOZTTrOEqSOA.

Using $R_{\mathrm{init}} \approx 2R_\odot$ (approximate stalling orbital separation of the secondary across our models), $\Delta M \approx 5M_\odot$ (the entire mass of the envelope), $v_{\mathrm{ej}} \approx 18$ km/s (the velocity at $10R_\odot$ at the end of our simulation), $\kappa \approx 0.32$ cm^2 g, and $T_{\mathrm{rec}} \approx 4500$ K, we find $L_{\mathrm{p}} \approx 10^{37}$ erg s^{-1}, $t_{\mathrm{p}} \approx 274$ d, and $E_{\mathrm{rad,p}} \approx 2 \times 10^{44}$ erg.

C. MESA PROFILES

Here we provide more detail on the 1D stellar models (the initial conditions for the 3D hydrodynamics) built in MESA. Our primary is constructed using the setup of Götberg et al. (2018), but for a single star. The top row of Figure 10 shows density profiles (vs. radius and mass coordinate) for the three models we simulate in 3D hydrodynamics. The bottom left panel shows the mass enclosed vs. radius. We also compare to the primary from the 1D MESA study of CE ejection of Fragos et al. (2019), which was $12M_\odot$ and $\approx 500R_\odot$. The density profiles are all very similar, being highly centrally concentrated with a core of $\approx 5M_\odot$ sequestered at $\lesssim 1R_\odot$. The greatest difference is in the inner $0.1R_\odot$, where the least centrally concentrated model ($750R_\odot$) has a central density of $\rho_c \approx 10^3$ g/cm^3 and the most centrally concentrated model ($1080R_\odot$) has a central density of $\rho_c \approx 10^6$ g/cm^3. The density drops from a central value of $\rho_c \approx 10^3$–10^6 g/cm^3 to $\rho \lesssim 10^{-5}$ g/cm ^{3} by $R = 10R_\odot$.

The bottom right panel of Figure 10 shows the 1D composition profiles for hydrogen, helium, carbon, and nitrogen at the beginning of the simulation (thus, they are identical to the MESA composition profiles) for the $900R_\odot$ star. See Figure 5 for 3D renderings of the chemical abundance of the system as a function of time. Note that the abrupt
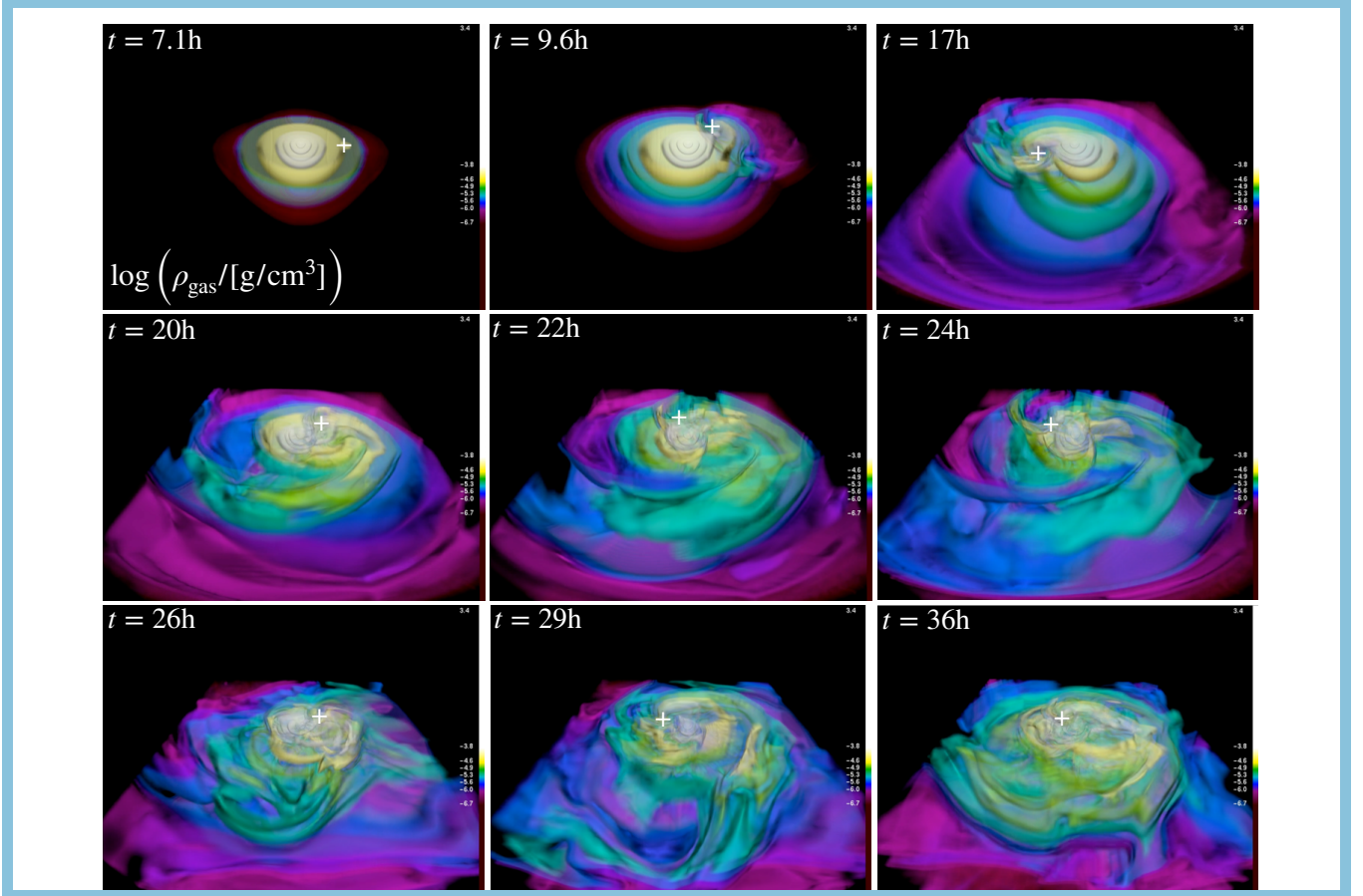
Figure 7. Video figure (viewable online). Video shows a 3D rendering of the logarithm of gas density for the full domain (compare to Figure 6) during the neutron star's inspiral for the ($900R_\odot$, $v_i = v_{\text{integrator}}$) run. Shells correspond to different density isosurfaces; white is highest density, dark purple is lowest density. Video highlights the severely shocked and disturbed density structure of the outer envelope, which is ejected as the neutron star orbits the giant star. Position of the neutron star is indicated by the white '+'. Videos also available at https://youtube.com/channel/UCShahcfGrj5dOZTTrOEqSOA.

changes in composition are a result of the well-defined compositional layering from the MESA model (this is mapped exactly into FLASH, thus this is the same as the MESA composition profile).

D. ADJUSTED 1D ENERGY FORMALISM

Here we provide more detailed results of our 1D energy formalism (method discussed in §2.2). Figure 11 shows binding and orbital energies vs. radius and mass for the three models from that we simulate in 3D hydrodynamics (see Figures 1, 10). In the 1st row we compare gravitational binding energy E_{grav} between all three models. In other rows we show detailed results for each model including binding energy from the standard α formalism (E_{grav}), the Bondi radius adjusted formalism ($E_{\text{grav,R}_a}$), the Roche radius adjusted formalism ($E_{\text{grav,R}_{\text{Roche}}}$), and the change in orbital energy (ΔE_{orb}). In general, we see that the binding energy profiles, similar to the density profiles (Figure 10), are also highly centrally concentrated and that $< 0.1\%$ of the binding energy is at radii larger than $10R_\odot$. The different calculated energies (for the standard α formalism and for the $r - R_a$ and $r - R_{\text{Roche}}$ adjusted formalism) are used to determine the predicted envelope ranges in the 1D energy formalism (see Section 2.2).

E. FORBIDDEN DONOR RADII

The star cannot fill its Roche lobe at an arbitrary moment in its evolution; it needs to have a size large enough such that it would not have filled its Roche lobe before. Simply including stellar ages where the star's radius exceeds any earlier radius it had is not sufficient, as the orbit is changing as well due to wind mass loss and possibly tidal interactions.
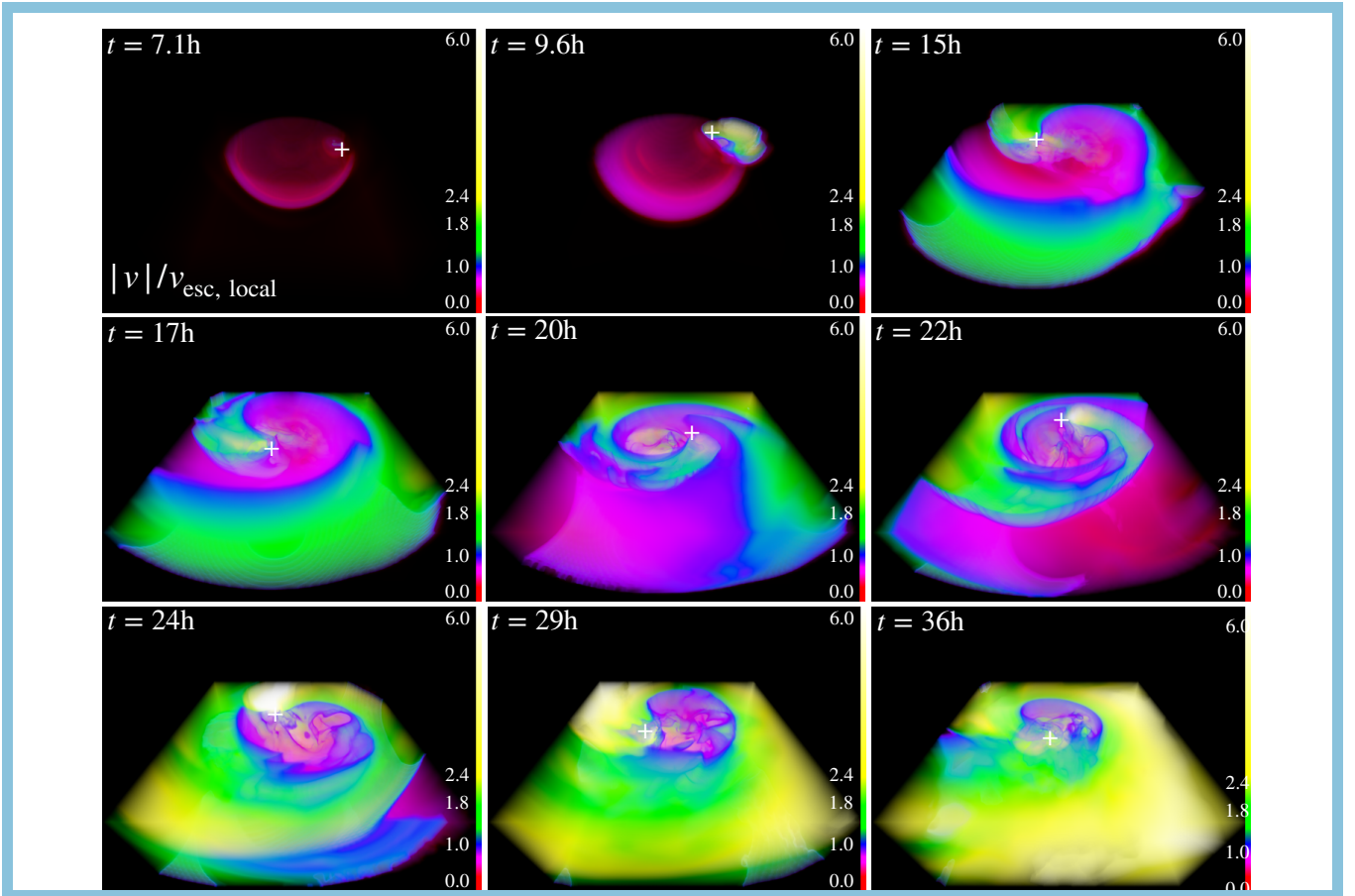
Figure 8. Video figure (viewable online). Video shows a 3D rendering of the ratio of velocity magnitude to local escape velocity for the full domain for the $(900R_\odot, v_i = v_{\text{integrator}})$ run. Blue isosurface is at $|v|/v_{\text{esc,local}} = 1$, pink-red is < 1, green-yellow is > 1. Position of the neutron star is indicated by the white '+'. Videos also available at https://youtube.com/channel/UCShahcfGrj5dOZTTrOEqSOA.

A standard assumption is to think about the orbital changes in the Jeans mode approximation, where the orbital change is a very simple function of the mass loss. It relies on the assumption that (i) mass loss is steady (i.e., in a smooth wind, not a sudden supernova explosion) and (ii) it is lost with a velocity that is high compared to the orbital velocities (such that, e.g., it cannot have any tidal interaction with the system) and (iii) it is lost from the vicinity of the mass-losing star in a spherically symmetric fashion in the reference frame of the mass-losing star.

This gives the following simple analytical result that $a \times (M_1 + M_2) = \text{constant}$. In this work, this means that any time t the separation $a(t)$ is the following function of the masses and initial parameters:

$$a(t) = a(t = 0) \times \frac{M_d(t = 0) + M_{NS}}{M_d(t) + M_{NS}} \tag{E4}$$

We calculate the size of the Roche radius of a system with an initial separation of $a = 1301R_\odot$—this is the initial separation of the widest system to fill its Roche lobe on the first ascent. The system widens with time due to the Jeans mode mass loss. A system with an initial separation slightly larger than $a = 1301R_\odot$ would fill its Roche lobe on the second ascent. But because of mass loss, the system will have widened in the meantime and the star needs to be $R_\star = 900R_\odot$ or larger. The star can thus not fill its Roche lobe for ages between $t(R = 757R_\odot)$ and $t(R = 900R_\odot)$, between the first peak and the second rise (see Figure 1).

In practice this means that the stellar models available to us in this work are: (a) stars that fill their Roche lobe on the first ascent, that is with radius smaller than $757R_\odot$, and (b) stars that fill their Roche lobe on the second ascent, provided their radius is larger than $900R_\odot$. In other words, we avoid using models with "forbidden radii" (radii between 757–900$R_\odot$).
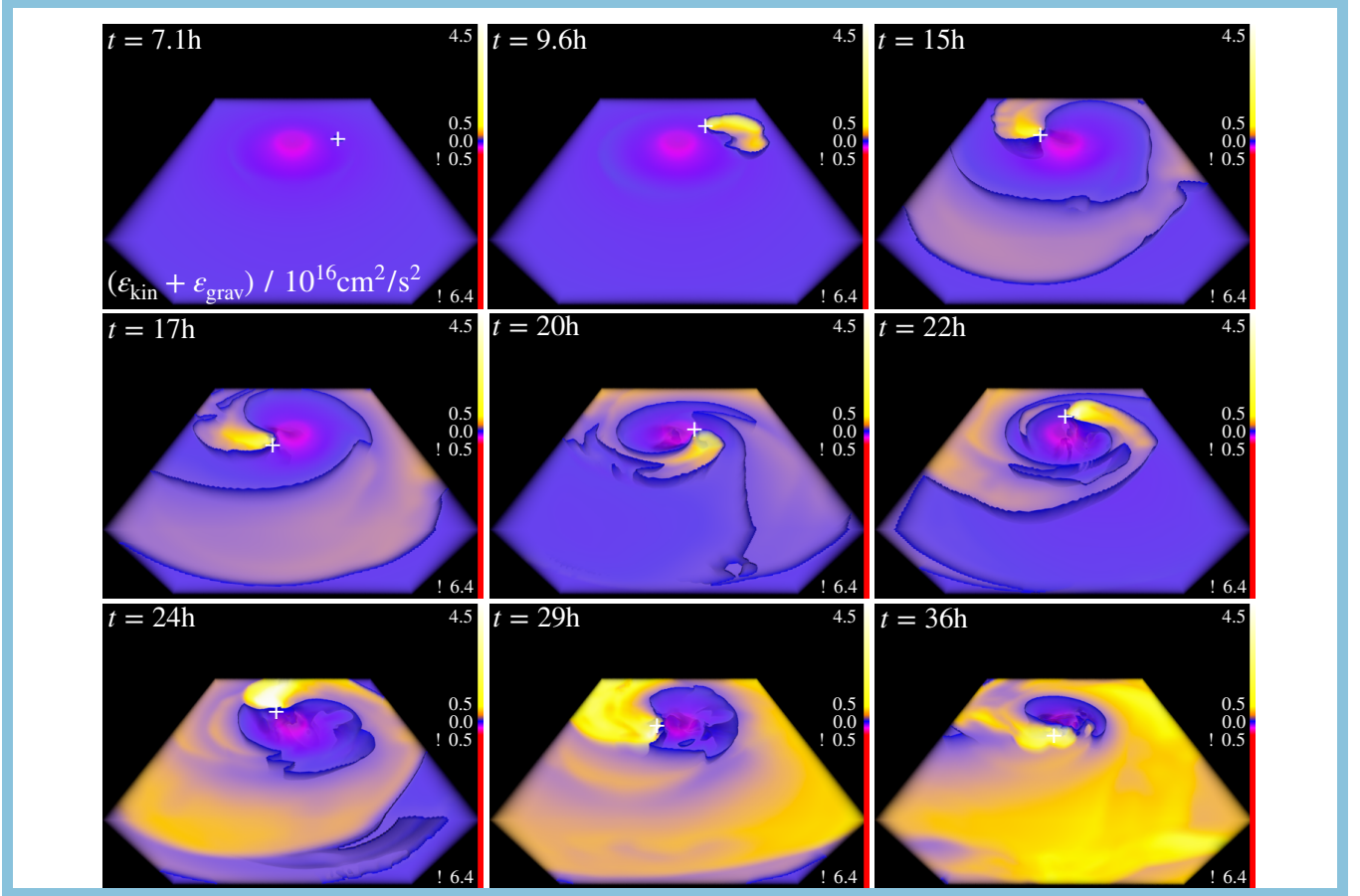
Figure 9. Video figure (viewable online). Video shows a 3D rendering of the sum of specific kinetic and potential energy for the full domain for the $(900R_\odot, v_i = v_{\mathrm{integrator}})$ run. Blue isosurface at $\varepsilon = 0$, pink-purple corresponds to bound $(\varepsilon < 0)$ and yellow corresponds to unbound $(\varepsilon > 0)$. Position of the neutron star is indicated by the white '+'. Videos also available at https://youtube.com/channel/UCShahcfGrj5dOZTTrOEqSOA.

F. MERGER TIME DISTRIBUTION

In order to estimate the merger time distributions of these binary neutron star systems, we take a linear distribution in separations before the supernova (SN) from 1.1–$2.8R_\odot$. We then take each separation and run 1000 randomly oriented kicks. We take kick magnitudes of 100 km/s, 250 km/s (this is a typical value; e.g., Hobbs et al. 2005), and 500 km/s and the final mass of the new neutron star after the SN is $1.4M_\odot$. To calculate the post-SN orbit we use Eqns. (7) and (8) of Andrews & Zezas (2019) and to calculate the merger times of these post-SN orbits we use Peters (1964). Figure 12 shows the merger time distribution of the two resulting neutron stars for supernova kick velocities of 100 km/s, 250 km/s, and 500 km/s. For the 250km/s kick, the surviving fraction of binaries is $\approx 45\%$. After supernova kicks, we calculate that these systems will form binary neutron stars that merge within 0.01–1 Gyr (95% confidence interval of the probability distribution for the 250 km/s kick). We caution the reader that after envelope ejection we expect a stable mass transfer phase to occur that will likely tighten the binary (see, e.g., Vigna-Gómez et al. 2020). As such, this figure should be taken as a robust upper limit for the merger timescale.

G. NUMERICAL CONVERGENCE

Here we present a brief numerical convergence study of the effect of numerical diffusion on the simulation results. The 1st row of Figure 13 shows trajectories and orbital separation vs. time for two different resolution criteria for the $(900R_\odot, v_i = v_{\mathrm{integrator}})$ run. We use the same refinement criteria but two different box sizes: $\Delta X_{\max} = (100R_\odot, 40R_\odot)$, translating to a factor of 2.5X increase in linear resolution between the two simulations. The secondary does not inspiral as deeply for the higher resolution run. The higher resolution run stalls and attains a final orbital separation of $a_{\mathrm{f}} \approx 3.1R_\odot$, while the lower resolution run attains a final orbital separation of $a_{\mathrm{f}} \approx 2.8R_\odot$.
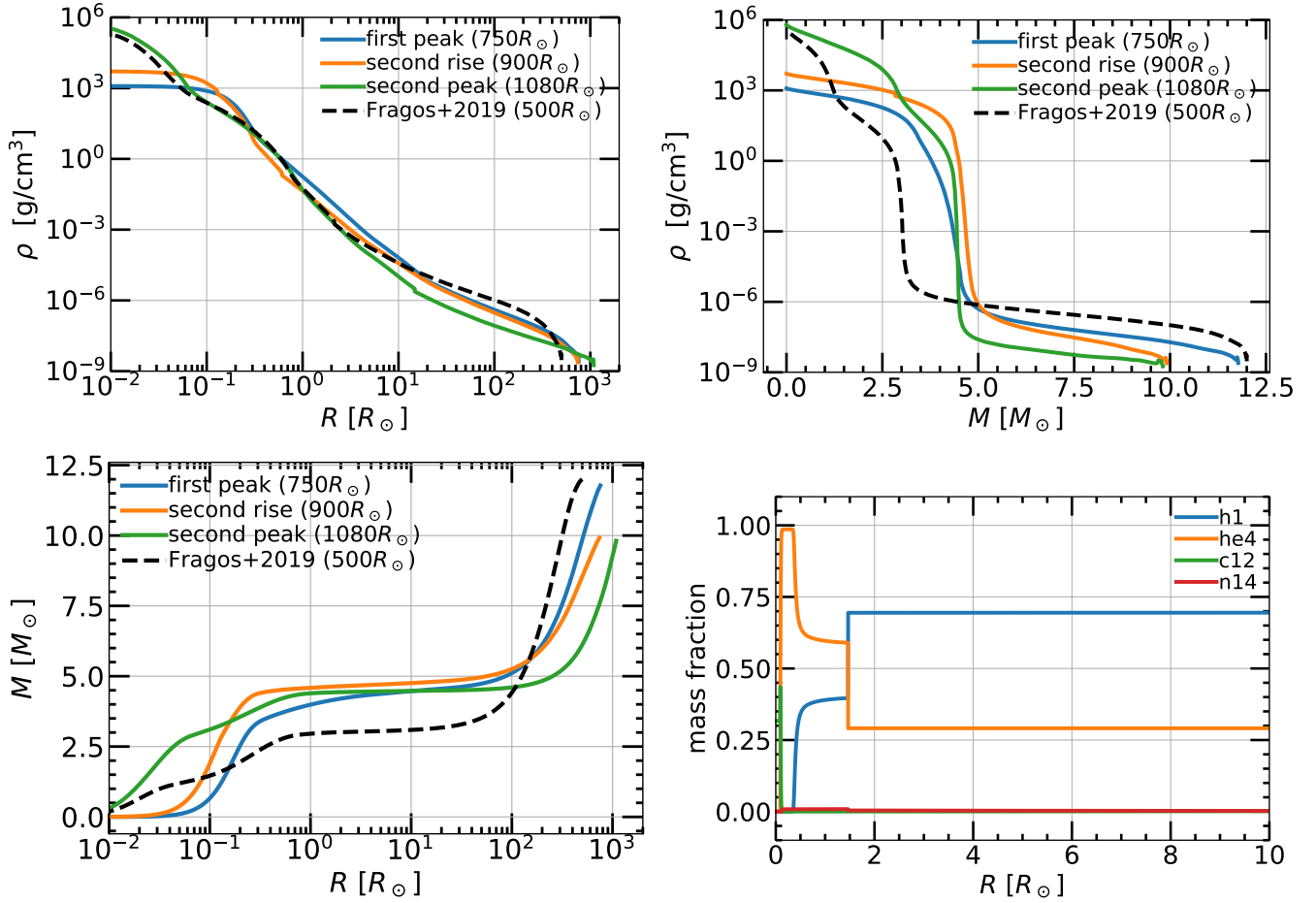
Figure 10. Top: MESA density profiles vs. radius and mass coordinate for the three models that we simulate in 3D hydrodynamics (see Figure 1) and for the primary from Fragos et al. (2019). Bottom left: enclosed mass vs. radius. Bottom right: initial 1D composition profiles of hydrogen, helium, carbon, and nitrogen for the $900R_\odot$ star.

The 2nd row of Figure 13 shows the density profile along one direction in the orbital plane (other directions are similar) at a few different times throughout the simulation for the same two runs. For reference, the relaxation process is $t_{\rm relax} \approx 100 t_{\rm dyn,core} \approx 6$ hr. After relaxation onto the grid, the central density decreases by a factor of ≈ 5. The lower resolution run ($\Delta X_{\rm max} = 100R_\odot$) shows lower core densities at radii of ($r < 1R_\odot$) and higher densities at radii of $r > 1R_\odot$, especially at later times, whereas the higher resolution run conserves its density profile to late times. This mass leakage from the core in the lower resolution run leads to a higher envelope density and thus a higher drag force (as $F_{\rm drag} \propto \rho$) for the lower resolution run. This likely explains its slightly deeper inspiral.

The 3rd row of Figure 13 shows mass enclosed vs. time at several radii for the same two runs. The $\Delta X_{\rm max} = 40R_\odot$ run conserves the inner mass shells much better than the $\Delta X_{\rm max} = 100R_\odot$ run. However, for both runs, while the innermost core expands and the mass spreads to somewhat larger radii, this has no effect on the secondary's orbit as the orbital separation is always at least $r \gtrsim 1R_\odot$, whereas the mass is redistributed within $r \lesssim 0.5R_\odot$.

REFERENCES

Abbott, B. P., Abbott, R., Abbott, T. D., et al. 2020, ApJL, 892, L3, doi: 10.3847/2041-8213/ab75f5

Abbott, B. P., Abbott, R., Abbott, T. D., & Acernese, F. e. a. 2017a, ApJL, 848, L13, doi: 10.3847/2041-8213/aa920c

—. 2017b, ApJL, 848, L12, doi: 10.3847/2041-8213/aa91c9

Andrews, J. J., & Zezas, A. 2019, MNRAS, 486, 3213, doi: 10.1093/mnras/stz1066
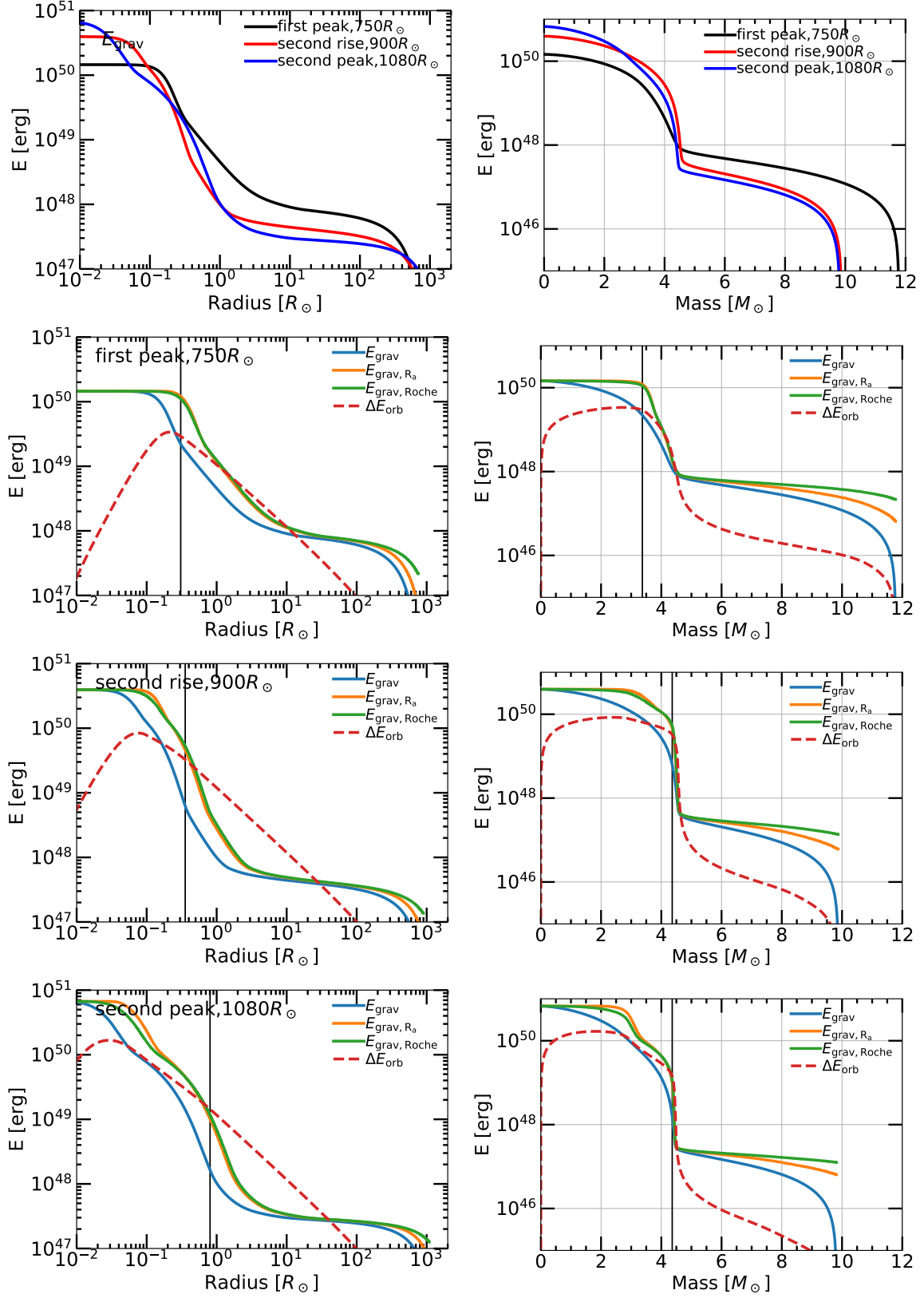
Figure 11. Absolute value of binding and orbital energies vs. radius and mass for the three models we simulate in 3D hydrodynamics (see Figure 1). Top: comparison of the binding energy E_{grav} between all three models. Other rows: detailed results for each model, including binding energies from the standard α formalism (E_{grav}), the Bondi radius adjusted formalism ($E_{\mathrm{grav,R_a}}$), the Roche radius adjusted formalism ($E_{\mathrm{grav,R_{Roche}}}$), and the change in orbital energy (ΔE_{orb}). Vertical line indicates radius of the core (defined by `he_core_mass` attribute in MESA).
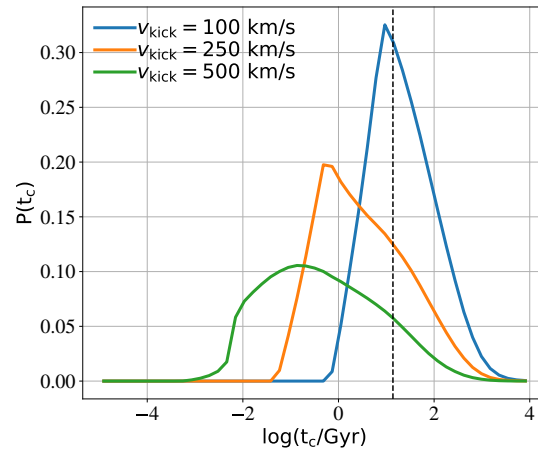
Figure 12. Merger time distribution of the two resulting neutron stars for supernova kick velocities of 100 km/s, 250 km/s (this is a typical value Hobbs et al. 2005), and 500 km/s. Dashed line indicates the age of the Universe.
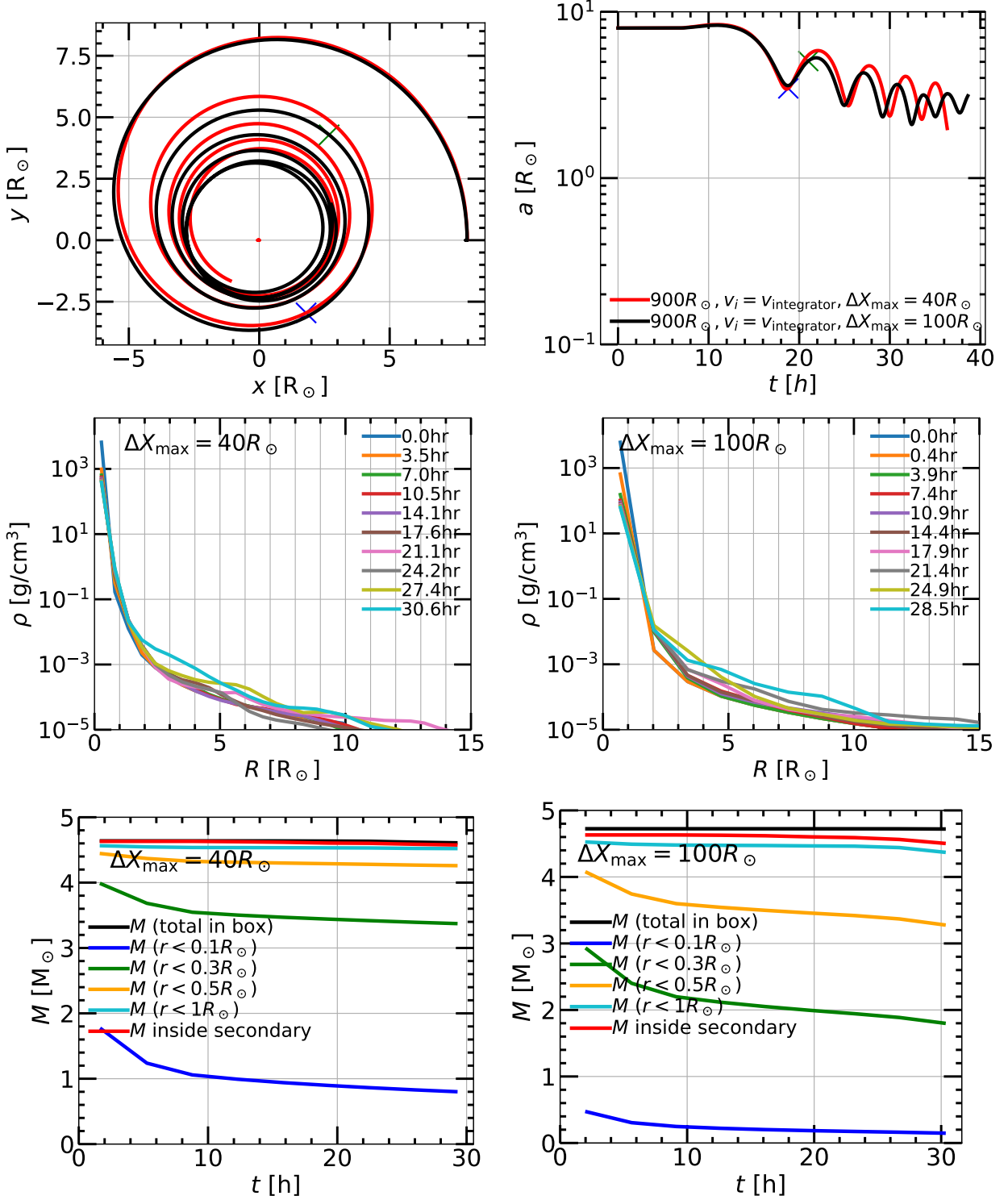
Figure 13. Numerical convergence study. 1st row: orbital separation vs. time for the $(900R_\odot, v_i = v_{\text{integrator}})$ run, with box size $\Delta X_{\text{max}} = 100R_\odot$ (black) and $\Delta X_{\text{max}} = 40R_\odot$ (red, 2.5X linear resolution of other simulation) on a side. Green and blue 'X's mark the time at which the envelope is ejected for the black and red lines respectively (see Figure 4). 2nd row: density profile along one direction in FLASH as a function of time. Left panel is the $\Delta X_{\text{max}} = 40R_\odot$ run and right panel is the $\Delta X_{\text{max}} = 100R_\odot$ run. 3rd row: mass enclosed vs. time at several radii as a function of time.

Asplund, M., Grevesse, N., Sauval, A. J., & Scott, P. 2009,
    ARA&A, 47, 481,
    doi: 10.1146/annurev.astro.46.060407.145222

Astropy Collaboration, Robitaille, T. P., Tollerud, E. J.,
    et al. 2013, A&A, 558, A33,
    doi: 10.1051/0004-6361/201322068

Astropy Collaboration, Price-Whelan, A. M., Sipőcz, B. M.,
    et al. 2018, AJ, 156, 123, doi: 10.3847/1538-3881/aabc4f

Belczynski, K., Repetto, S., Holz, D. E., et al. 2016, ApJ,
    819, 108, doi: 10.3847/0004-637X/819/2/108

Blaauw, A. 1993, in Astronomical Society of the Pacific
    Conference Series, Vol. 35, Massive Stars: Their Lives in
    the Interstellar Medium, ed. J. P. Cassinelli & E. B.
    Churchwell, 207

Blagorodnova, N., Kotak, R., Polshaw, J., et al. 2017, ApJ,
    834, 107, doi: 10.3847/1538-4357/834/2/107

Bondi, H., & Hoyle, F. 1944, MNRAS, 104, 273,
    doi: 10.1093/mnras/104.5.273

Brott, I., de Mink, S. E., Cantiello, M., et al. 2011, A&A,
    530, A115, doi: 10.1051/0004-6361/201016113

Cantiello, M., Yoon, S. C., Langer, N., & Livio, M. 2007,
    A&A, 465, L29, doi: 10.1051/0004-6361:20077115

Chamandy, L., Blackman, E. G., Frank, A.,
    Carroll-Nellenback, J., & Tu, Y. 2020, MNRAS, 495,
    4028, doi: 10.1093/mnras/staa1273

Coulter, D. A., Foley, R. J., Kilpatrick, C. D., et al. 2017,
    Science, 358, 1556, doi: 10.1126/science.aap9811

Davis, A., Jones, S., & Herwig, F. 2019, MNRAS, 484,
    3921, doi: 10.1093/mnras/sty3415

De, S., MacLeod, M., Everson, R. W., et al. 2020, ApJ,
    897, 130, doi: 10.3847/1538-4357/ab9ac6

de Jager, C., Nieuwenhuijzen, H., & van der Hucht, K. A.
    1988, A&AS, 72, 259

de Kool, M. 1990, ApJ, 358, 189, doi: 10.1086/168974

de Mink, S. E., Langer, N., Izzard, R. G., Sana, H., & de
    Koter, A. 2013, ApJ, 764, 166,
    doi: 10.1088/0004-637X/764/2/166

Eggleton, P. P. 1983, ApJ, 268, 368, doi: 10.1086/160960

Everson, R. W. 2020, in prep.

Everson, R. W., MacLeod, M., De, S., Macias, P., &
    Ramirez-Ruiz, E. 2020, ApJ, 899, 77,
    doi: 10.3847/1538-4357/aba75c

Fragos, T., Andrews, J. J., Ramirez-Ruiz, E., et al. 2019,
    ApJL, 883, L45, doi: 10.3847/2041-8213/ab40d1

Fryxell, B., Olson, K., Ricker, P., et al. 2000, ApJS, 131,
    273, doi: 10.1086/317361

Goldstein, A., Veres, P., Burns, E., et al. 2017, ApJL, 848,
    L14, doi: 10.3847/2041-8213/aa8f41

Götberg, Y., de Mink, S. E., Groh, J. H., et al. 2018, A&A,
    615, A78, doi: 10.1051/0004-6361/201732274

Götberg, Y., Korol, V., Lamberts, A., et al. 2020, arXiv
    e-prints, arXiv:2006.07382.
    https://arxiv.org/abs/2006.07382

Guillochon, J., & Ramirez-Ruiz, E. 2013, ApJ, 767, 25,
    doi: 10.1088/0004-637X/767/1/25

Guillochon, J., Ramirez-Ruiz, E., Rosswog, S., & Kasen, D.
    2009, ApJ, 705, 844, doi: 10.1088/0004-637X/705/1/844

Heger, A., Fryer, C. L., Woosley, S. E., Langer, N., &
    Hartmann, D. H. 2003, ApJ, 591, 288,
    doi: 10.1086/375341

Hinkle, K. H., Lebzelter, T., Fekel, F. C., et al. 2020, arXiv
    e-prints, arXiv:2010.01081.
    https://arxiv.org/abs/2010.01081

Hirai, R., Podsiadlowski, P., & Yamada, S. 2018, ApJ, 864,
    119, doi: 10.3847/1538-4357/aad6a0

Hobbs, G., Lorimer, D. R., Lyne, A. G., & Kramer, M.
    2005, MNRAS, 360, 974

Howitt, G., Stevenson, S., Vigna-Gómez, A. r., et al. 2020,
    MNRAS, 492, 3229, doi: 10.1093/mnras/stz3542

Hoyle, F., & Lyttleton, R. A. 1939, Proceedings of the
    Cambridge Philosophical Society, 35, 405,
    doi: 10.1017/S0305004100021150

Hunter, J. D. 2007, Computing in Science and Engineering,
    9, 90, doi: 10.1109/MCSE.2007.55

Hut, P. 1981, A&A, 99, 126

Iben, Icko, J., & Livio, M. 1993, PASP, 105, 1373,
    doi: 10.1086/133321

Ivanova, N., Justham, S., Avendano Nandez, J. L., &
    Lombardi, J. C. 2013a, Science, 339, 433,
    doi: 10.1126/science.1225540

Ivanova, N., Justham, S., Chen, X., et al. 2013b, A&A Rv,
    21, 59, doi: 10.1007/s00159-013-0059-2

Kasen, D., Metzger, B., Barnes, J., Quataert, E., &
    Ramirez-Ruiz, E. 2017, Nature, 551, 80,
    doi: 10.1038/nature24453

Kasen, D., & Ramirez-Ruiz, E. 2010, ApJ, 714, 155,
    doi: 10.1088/0004-637X/714/1/155

Kasen, D., & Woosley, S. E. 2009, ApJ, 703, 2205,
    doi: 10.1088/0004-637X/703/2/2205

Kippenhahn, R., & Weigert, A. 1967, ZA, 65, 251

Kramer, M., Schneider, F. R. N., Ohlmann, S. T., et al.
    2020, A&A, 642, A97, doi: 10.1051/0004-6361/202038702

Kruckow, M. U., Tauris, T. M., Langer, N., et al. 2016,
    A&A, 596, A58, doi: 10.1051/0004-6361/201629420

Lauterborn, D. 1970, A&A, 7, 150

Law-Smith, J., Guillochon, J., & Ramirez-Ruiz, E. 2019,
    ApJL, 882, L25, doi: 10.3847/2041-8213/ab379a

Law-Smith, J. A. P., Coulter, D. A., Guillochon, J.,
    Mockler, B., & Ramirez-Ruiz, E. 2020, arXiv e-prints,
    arXiv:2007.10996. https://arxiv.org/abs/2007.10996

Livio, M., & Soker, N. 1988, ApJ, 329, 764,
 doi: 10.1086/166419

MacLeod, M., Antoni, A., Murguia-Berthier, A., Macias,
 P., & Ramirez-Ruiz, E. 2017a, ApJ, 838, 56,
 doi: 10.3847/1538-4357/aa6117

MacLeod, M., Macias, P., Ramirez-Ruiz, E., et al. 2017b,
 ApJ, 835, 282, doi: 10.3847/1538-4357/835/2/282

MacLeod, M., & Ramirez-Ruiz, E. 2015, ApJ, 803, 41,
 doi: 10.1088/0004-637X/803/1/41

Mason, E., Diaz, M., Williams, R. E., Preston, G., &
 Bensby, T. 2010, A&A, 516, A108,
 doi: 10.1051/0004-6361/200913610

Moe, M., & Di Stefano, R. 2017, ApJS, 230, 15,
 doi: 10.3847/1538-4365/aa6fb6

Mohamed, S., & Podsiadlowski, P. 2007, in Astronomical
 Society of the Pacific Conference Series, Vol. 372, 15th
 European Workshop on White Dwarfs, ed. R. Napiwotzki
 & M. R. Burleigh, 397

Mould, J., Cohen, J., Graham, J. R., et al. 1990, ApJL,
 353, L35, doi: 10.1086/185702

Nandez, J. L. A., & Ivanova, N. 2016, MNRAS, 460, 3992,
 doi: 10.1093/mnras/stw1266

Nicholls, C. P., Melis, C., Soszynski, I., et al. 2013,
 MNRAS, 431, L33, doi: 10.1093/mnrasl/slt003

Ohlmann, S. T., Röpke, F. K., Pakmor, R., & Springel, V.
 2016, ApJL, 816, L9, doi: 10.3847/2041-8205/816/1/L9

Paczynski, B. 1976, in Structure and Evolution of Close
 Binary Systems, ed. P. Eggleton, S. Mitton, &
 J. Whelan, Vol. 73, 75

Paxton, B., Bildsten, L., Dotter, A., et al. 2011, ApJS, 192,
 3, doi: 10.1088/0067-0049/192/1/3

Paxton, B., Cantiello, M., Arras, P., et al. 2013, ApJS, 208,
 4, doi: 10.1088/0067-0049/208/1/4

Paxton, B., Marchant, P., Schwab, J., et al. 2015, ApJS,
 220, 15, doi: 10.1088/0067-0049/220/1/15

Peters, P. C. 1964, Physical Review, 136, 1224,
 doi: 10.1103/PhysRev.136.B1224

Popov, D. V. 1993, ApJ, 414, 712, doi: 10.1086/173117

Prust, L. J., & Chang, P. 2019, MNRAS, 486, 5809,
 doi: 10.1093/mnras/stz1219

Renzo, M., Ott, C. D., Shore, S. N., & de Mink, S. E. 2017,
 A&A, 603, A118, doi: 10.1051/0004-6361/201730698

Ricker, P. M., & Taam, R. E. 2008, ApJL, 672, L41,
 doi: 10.1086/526343

—. 2012, ApJ, 746, 74, doi: 10.1088/0004-637X/746/1/74

Ricker, P. M., Timmes, F. X., Taam, R. E., & Webbink,
 R. F. 2019, IAU Symposium, 346, 449,
 doi: 10.1017/S1743921318007433

Ritter, H. 1975, Mitteilungen der Astronomischen
 Gesellschaft Hamburg, 36, 93

Robertson, B. E., Kravtsov, A. V., Gnedin, N. Y., Abel, T.,
 & Rudd, D. H. 2010, MNRAS, 401, 2463,
 doi: 10.1111/j.1365-2966.2009.15823.x

Sana, H., de Mink, S. E., de Koter, A., et al. 2012, Science,
 337, 444, doi: 10.1126/science.1223344

Sand, C., Ohlmann, S. T., Schneider, F. R. N., Pakmor, R.,
 & Roepke, F. K. 2020, arXiv e-prints, arXiv:2007.11000.
 https://arxiv.org/abs/2007.11000

Sandquist, E. L., Taam, R. E., Chen, X., Bodenheimer, P.,
 & Burkert, A. 1998, ApJ, 500, 909, doi: 10.1086/305778

Staff, J. E., De Marco, O., Macdonald, D., et al. 2016,
 MNRAS, 455, 3511, doi: 10.1093/mnras/stv2548

Tauris, T. M., Kramer, M., Freire, P. C. C., et al. 2017,
 ApJ, 846, 170, doi: 10.3847/1538-4357/aa7e89

Timmes, F. X., & Swesty, F. D. 2000, ApJS, 126, 501,
 doi: 10.1086/313304

Turk, M. J., Smith, B. D., Oishi, J. S., et al. 2011, ApJS,
 192, 9, doi: 10.1088/0067-0049/192/1/9

Tutukov, A., & Yungelson, L. 1973, Nauchnye Informatsii,
 27, 70

Tutukov, A. V., & Yungelson, L. R. 1993, MNRAS, 260,
 675, doi: 10.1093/mnras/260.3.675

van den Heuvel, E. P. J. 1976, in Structure and Evolution
 of Close Binary Systems, ed. P. Eggleton, S. Mitton, &
 J. Whelan, Vol. 73, 35

Vigna-Gómez, A., MacLeod, M., Neijssel, C. J., et al. 2020,
 PASA, 37, e038, doi: 10.1017/pasa.2020.31

Vink, J. S., de Koter, A., & Lamers, H. J. G. L. M. 2001,
 A&A, 369, 574, doi: 10.1051/0004-6361:20010127

Webbink, R. F. 1984, ApJ, 277, 355, doi: 10.1086/161701

Wolf, B., & Schwab, J. 2017, Wmwolf/Py_Mesa_Reader:
 Interact With Mesa Output, 0.3.0, Zenodo,
 doi: 10.5281/zenodo.826958

Wu, S., Everson, R. W., Schneider, F. R. N.,
 Podsiadlowski, P., & Ramirez-Ruiz, E. 2020, ApJ, 901,
 44, doi: 10.3847/1538-4357/abaf48

Ye, C. S., Fong, W.-f., Kremer, K., et al. 2020, ApJL, 888,
 L10, doi: 10.3847/2041-8213/ab5dc5

Zhang, W., & Fryer, C. L. 2001, ApJ, 550, 357,
 doi: 10.1086/319734